Inferring 3D Ellipsoids based on Cross-Sectional Images with Applications to Porosity Control of Additive Manufacturing

Jianguo Wu[1*], Yuan Yuan[2], Haijun Gong[3], Tzu-Liang (Bill) Tseng[4]

[1*] *Department of Industrial Engineering and Management, Peking University, Beijing, China, 100871*
E-mail: jwu@coe.pku.edu.cn

[2] *IBM Research, Singapore 18983*

[3] *Department of Manufacturing Engineering, Georgia Southern University, Statesboro, GA 30458, USA*

[4] *Department of Industrial, Manufacturing and Systems Engineering, University of Texas at El Paso, TX 79968, USA*

Abstract

This paper develops a series of statistical approaches to inferring size distribution, volume number density and volume fraction of 3D ellipsoidal particles based on 2D cross-sectional images. Specifically, this paper first establishes an explicit linkage between the size of ellipsoidal particles and the size of cross-sectional elliptical contours. Then an efficient Quasi-Monte Carlo EM algorithm is developed to overcome the challenge of 3D size distribution estimation based on the established complex linkage. The relationship between the 3D and 2D particle number densities is also identified to estimate the volume number density and volume fraction. The effectiveness of the proposed method is demonstrated through simulation and case studies.

KEY WORDS: Ellipsoid Intersection; Quasi-Monte Carlo; Expectation Maximization; Additive manufacturing; Porosity.

1. INTRODUCTION

This paper develops a novel inspection method to infer the three-dimensional (3D) size distribution, volume number density (number per unit volume), and volume fraction (volume percentage) of ellipsoidal particles in materials based on 2D cross-sectional microscopic images. Although recent development of measurement technology makes the direct measurement of 3D particles possible, indirect measurement from lower dimension are still widely used for practical reasons. One motivating application example is the measurement of void (considered as a special type of particle) defects in the metal-based additive manufacturing. The porosity is one of the most common and critical quality issues in metal-based additive manufacturing, especially in structural or load-bearing applications [1-4]. It refers to the presence of defects in the form of void or simply a lack

of solid material, as shown in Figure 1 (bottom panel) [3-6]. The formed pores or voids could serve as crack nucleation and propagation source, and thus reduce material stiffness, bending strength, hardness, and fatigue life [7-9]. Therefore the void size distribution and porosity (volume fraction of voids) need to be inspected for quality control and process optimization. Another example is the examination of the dispersion of reinforcing nanoparticles in composite manufacturing process [10-13]. One critical quality issue in the composite manufacturing is that due to high surface energy and poor wettability in molten metal, nanoparticles tend to agglomerate and form big clusters (Figure 1, top panel), which greatly limits their effectiveness in mechanical property enhancement. Therefore it is important to measure the size distribution, volume number density and volume percentage of nanoparticle *clusters* to characterize the product quality. Directly measuring the 3D size and volume percentage of particles is often very difficult, if not impossible. Microscopic images have been naturally used for examining microstructures and quality inspection. However, microscopic images only provide two-dimensional (2D) cross sections of materials, and are not always sufficient to characterize the material properties without knowing the three-dimensional information. Therefore, extracting 3D size distribution and volume percentage based on 2D cross-sectional measurement is highly desirable.

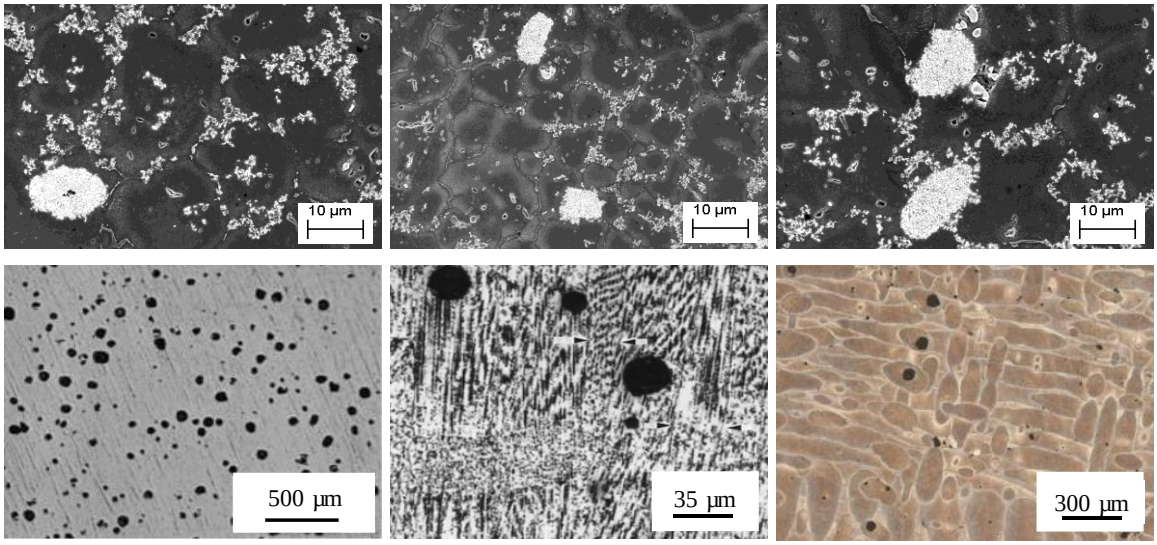

Figure 1. Microscopic images for metal matrix nanocomposites showing big particle clusters (top) [11] and metal-based AM products showing pores or voids (bottom) [3, 5, 6].

Revealing 3D particle information through cross-sectional images has been studied in image processing [14] and microstructural analysis, e.g., metal matrix nanocomposites [15-17]. However,

all of these studies assume the shape of particles to be spherical, which is too restricted and may not be realistic in many applications. For example, in the metal-based additive manufacturing, most voids within cross-sectional images show elliptical contours [4]. In this paper, we use a more general and flexible geometric shape — ellipsoid to represent the shape of particles. Compared with spherical case, inferring the size and volume number density of ellipsoids in 3D space based on only 2D cross-sectional images is much more complicated. Four fundamental questions need to be addressed: (1) what is the geometric size linkage between 3D ellipsoids and 2D cross-sectioned particles? (2) how to infer the size distribution of ellipsoidal particles from observed 2D particle sizes? (3) how to estimate the total volume fraction? and (4) how large cross-sectional images or how many cross-sectioned particles are needed to reach a certain estimation accuracy? This paper develops a series of approaches to address these questions. More specifically, an explicit geometry and size linkage between 3D ellipsoids and 2D cross-sectioned contours is established, which is a prerequisite for subsequent inferences. Then, a Quasi-Monte Carlo Expectation Maximization (QMC-EM) algorithm is developed to infer 3D size distribution based on observed 2D particles. The relationship between 3D and 2D particle number density is established through a nonhomogeneous Poisson Process, which being combined with the size distribution estimation, is used to infer the total volume fraction of particles in products. We also provide a theoretical foundation for the commonly used area fraction method for volume fraction estimation by proving that the area fraction of the cross-sectional ellipses is actually an unbiased estimator of the mean volume fraction.

The rest of this paper is organized as follows. Section 2 presents the detailed problem formulation and assumptions. The linkage on geometry and size between 3D ellipsoids and 2D particles, and the size estimation are provided in Section 3. In Section 4, a statistical approach is developed to estimate the volume number density and volume fraction. The simulation study and real case study in metallic additive manufacturing are provided in Section 5 and 6 respectively to evaluate the effectiveness of the proposed method. Section 7 is the conclusion and discussion.

2. PROBLEM FORMULATION AND ASSUMPTIONS

In microstructural analysis, specimens are first sectioned and then the cutting surfaces are polished to get microscopic images. Therefore a 2D microscopic image can be modelled as a cross-section resulted when a cutting plane intersects the specimen. As illustrated in Figure 2, if a particle

intersects with the image plane, it will display on the image; otherwise, it will not be captured by the image. Figure 3 shows particles scattered in 3D space and three randomly sampled microscopic images with intersected 2D particle contours. With this inspection scheme, the problem facing us is that based on the size and number of observed particles in 2D images, how we can infer the 3D particle information, including size distribution, particle volume number density and volume fraction.

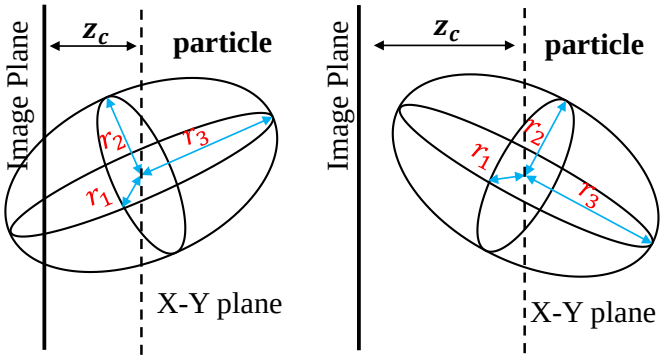

Figure 2. A particle shown (left) and not shown (right) on the image.

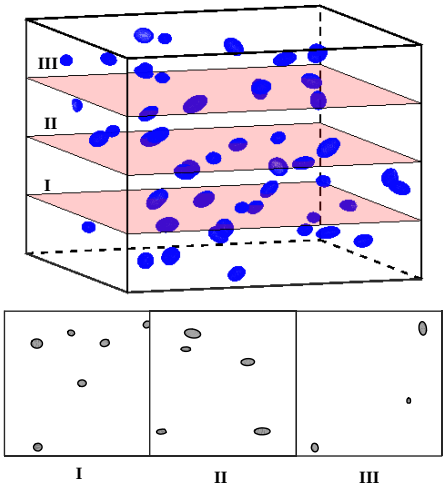

Figure 3. 3D distribution of particles and three cross-sectional images showing 2D particle contours

The above problem is intractable in general and certain assumptions need to be made. In this paper, we adopt one widely used assumption in spatial point pattern analysis and add another two assumptions specific to our problem as follows:

(i) The ellipsoidal particles are uniformly distributed in the 3D space of specimens with *complete spatial randomness* (CSR), where all particles follow a homogeneous Poisson

distribution and are independent of each other. CSR has been widely used to model spatial uniformity in point pattern analysis [16, 18]. It is the most fundamental assumption in the stereological analysis [14], without which the statistical inference of 3D particles based on 2D sections is almost impossible.

(ii) All the particles are in ellipsoidal shape with semi-principal axes of length r_1, r_2 and r_3 where r_1, r_2 and r_3 are continuous random variables and $r_1 \leq r_2 \leq r_3$. This assumption is more general than spherical shapes, where the latter is just a special case of the former with equal semi-principal axes. This assumption is also more realistic, as in nanocomposites or additive manufacturing, perfectly spherical particles or pores are rare. The circularity and elongation of the intersected contours [4] indicate that ellipsoid is more accurate in approximating the shape of particles.

(iii) The orientations of three principal axes of ellipsoidal particles are uniformly distributed in 3D space. This assumption indicates that if a particle is intersected, it could be cut by the image plane at any location and orientation with equal possibility.

With these assumptions, the following sections will introduce our statistical approaches to inferring the size distribution, volume number density and volume fraction of particles based on cross-sectional images.

3. INFERRING THE SIZE DISTRIBUTION OF 3D ELLIPSODIAL PARTICLES

3.1 Intersection of an Ellipsoid with an Arbitrary Plane

To infer the size distribution of ellipsoids, it is essential to link the 2D sizes of the cross-sectioned contours with 3D sizes of ellipsoids. For a spherical particle, circle equation of the intersection can be obtained intuitively. However, the analytical equation for the intersection of an ellipsoid by an arbitrary plane is very complicated. Note that the problem of cutting a standard ellipsoid (principal axes overlapping with X, Y and Z axis) by an arbitrary plane is equivalent to cutting an arbitrarily oriented ellipsoid with a horizontal plane. We derived the analytical equation to establish that linkage in Theorem 1 as follows.

Theorem 1: Suppose an ellipsoid is centered at the origin of the Cartesian coordinate system with semi-principal axes $\boldsymbol{r_i}$ of length $r_i, i = 1,2,3$ where $r_1 \leq r_2 \leq r_3$, as shown in Figure 4. The

orientation of each axis is represented by two angles $p_i \in (-\frac{\pi}{2}, \frac{\pi}{2}]$ and $\theta_i \in (-\pi, \pi]$, where p_i is the angle between the i-th axis and XY plane (horizontal plane), and θ_i is the angle between the projection of the i-th axis in the XY plane and the x-axis ($i = 1, 2, 3$). The ellipsoid is cut by a horizontal cutting plane P_c of distance z_c ($z_c \geq 0$) to the XY plane. Then

(1) The cross section is an ellipse;

(2) The major and minor diameters d_2 and d_1 ($d_1 \leq d_2$) of the ellipse are

$$d_{1,2}^2 = \frac{8\left(1 - \frac{z_c^2}{r_1^2 \sin^2 p_1 + r_2^2 \sin^2 p_2 + r_3^2 \sin^2 p_3}\right)}{\left(\frac{\cos^2 p_1}{r_1^2} + \frac{\cos^2 p_2}{r_2^2} + \frac{\cos^2 p_3}{r_3^2}\right) \pm \sqrt{\left(\frac{\cos^2 p_1}{r_1^2} + \frac{\cos^2 p_2}{r_2^2} + \frac{\cos^2 p_3}{r_3^2}\right)^2 - 4\left(\frac{\sin^2 p_1}{r_2^2 r_3^2} + \frac{\sin^2 p_2}{r_1^2 r_3^2} + \frac{\sin^2 p_3}{r_1^2 r_2^2}\right)}} \quad (1)$$

(3) The distance z_c satisfies the following constraint

$$z_c \leq z_u = \sqrt{r_1^2 \sin^2 p_1 + r_2^2 \sin^2 p_2 + r_3^2 \sin^2 p_3} \quad (2)$$

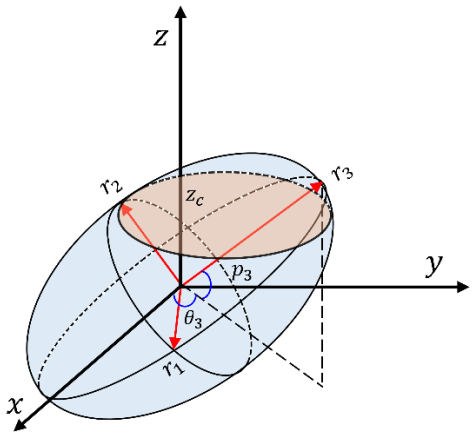

Figure 4. Illustration of an ellipsoid with three principal axes and intersected by an image plane parallel with XY plane.

The proof is given in Appendix A. It is well known that the cross section of an ellipsoid intersected by an arbitrary plane is an ellipse. However, the explicit size relationship between the intersectional ellipse and the corresponding ellipsoid in the general case is very difficult to derive. Hence, the size of the elliptical intersection is often calculated numerically. Klein [19] derived explicit formulas for the size relationship in the case of cutting a standard ellipsoid with an arbitrarily oriented plane. In this paper, however, we establish the linkage using a totally different

perspective for the case where an arbitrarily oriented ellipsoid is cut by a horizontal plane. The advantage of our notation and configuration lies in the convenience of direct statistical modeling of the orientation parameters and cutting process. From Equation (1) we can see that the size of the cross-sectional ellipse is independent of θ_i, which is straightforward since rotating the ellipsoid along the z-axis will not change the size of the intersection by a plane parallel with XY plane. Besides, if the ellipsoid is degenerated to a sphere of radius r, the ellipse is degenerated to a circle with diameter $d = 2\sqrt{r^2 - z_c^2}$, which can be easily obtained based on Equation (1) and the constraint $\sum_{i=1}^{3} \sin^2 p_i = 1$ (see Appendix A). Equation (2) gives the semi-height z_u of the ellipsoid or the maximum distance for the cutting plane to intersect with the ellipse centered at the origin. Based on this linkage, we can perform statistical inference on the size distribution of 3D ellipsoids given observed intersectional ellipses. The detail will be presented in the following subsections.

3.2 Size Inference and Parameter Estimation

Define $\boldsymbol{\theta}$ as the distribution parameters of the size (r_1, r_2, r_3) of the ellipsoid, $\{d_{i1}, d_{i2}, i = 1, \dots, n\}$ as the observed diameters of n intersectional ellipses, and let I_i denote a binary variable with $I_i = 1$ indicating that ellipsoid i is intersected by the image, then the problem is formulated as the estimation of $\boldsymbol{\theta}$ based on the observations $\{d_{i1}, d_{i2}, i = 1, \dots, n\}$. The distribution parameters are commonly estimated though maximum likelihood estimation (MLE). The likelihood function can be expressed as

$$L(\boldsymbol{\theta}|\{d_{i1}, d_{i2}, i = 1, \dots, n\}) = \prod_{i=1}^{n} f\,(d_{i1}, d_{i2}|\boldsymbol{\theta}, I_i = 1) \tag{3}$$

Due to the unobservable variables $(r_{i1}, r_{i2}, r_{i3}, p_{i1}, p_{i2}, p_{i3}, z_{ic})$, Equation (3) involves multiple integrations and is not analytically tractable. The expectation-maximization (EM) algorithm [20] is particularly effective in maximizing the likelihood function when the model depends on unobserved latent variables. In our model, there are 7 latent variables, out of which only 4 can be independent. If any four of them are known, the other three can be calculated using Equation (1) and (A. 6). Denote the hidden variable $\boldsymbol{h} = (r_1, r_2, r_3, p_3)$, then

$$f(d_{i1}, d_{i2}|\boldsymbol{\theta}, I_i = 1) = \int f(d_{i1}, d_{i2}|\boldsymbol{h}_i, I_i = 1)\, f(\boldsymbol{h}_i|\boldsymbol{\theta}, I_i = 1) d\boldsymbol{h}_i \tag{4}$$

However, due to the highly nonlinear relationship among $\boldsymbol{h}$, observations and other latent variables, the conditional expectation of the log-likelihood function is intractable, which makes the EM algorithm difficult to develop. In this article we first derived the complex complete-data likelihood function, and then proposed a Quasi-Monte Carlo based EM method (RQMC-EM) to estimate the size distribution parameters. The following subsections present the technical details.

3.2.1 Derivation of the Complete-data Likelihood Function

The complete-data likelihood function $L(\boldsymbol{\theta}|\boldsymbol{h}, d_1, d_2, I = 1)$ is essential in the development of the EM algorithm. It can be explicitly expressed as

$$f(\boldsymbol{h}, d_1, d_2|\boldsymbol{\theta}, I = 1) = f(\boldsymbol{h}|\theta, I = 1) f(d_1, d_2|\boldsymbol{h}, I = 1) \tag{5}$$

where

$$f(\boldsymbol{h}|\theta, I = 1) = f(p_3) f(r_1, r_2, r_3|\boldsymbol{\theta}) \frac{P(I = 1|r_1, r_2, r_3, p_3, \boldsymbol{\theta})}{P(I = 1|\boldsymbol{\theta})} \tag{6}$$

Suppose the upper bound of z_u is r_{max}, which is also the upper bound of r_3 and can be infinite, then

$$\begin{aligned} P(I = 1|\boldsymbol{\theta}) &= \int_0^{r_{max}} \frac{z_u}{r_{max}} f(z_u|\boldsymbol{\theta}) dz_u = \frac{E(z_u|\boldsymbol{\theta})}{r_{max}} \\ P(I = 1|r_1, r_2, r_3, p_3, \boldsymbol{\theta}) &= \int_0^{r_{max}} \frac{z_u}{r_{max}} f(z_u|r_1, r_2, r_3, p_3, \boldsymbol{\theta}) dz_u = \frac{E(z_u|r_1, r_2, r_3, p_3, \boldsymbol{\theta})}{r_{max}} \end{aligned} \tag{7}$$

Therefore

$$f(\boldsymbol{h}|\theta, I = 1) = f(p_3) f(r_1, r_2, r_3|\boldsymbol{\theta}) \frac{E(z_u|r_1, r_2, r_3, p_3, \boldsymbol{\theta})}{E(z_u|\boldsymbol{\theta})} \tag{8}$$

From Equation (6) and (8) we can see that the image cutting process is a biased sampling process where ellipsoids with larger height are more likely to be intersected by the image plane. Without considering such bias, the size would be overestimated. In Equation (8), $f(r_1, r_2, r_3|\boldsymbol{\theta})$ is given when the distribution of (r_1, r_2, r_3) is known. It is not intuitive to select an appropriate statistical distribution to model (r_1, r_2, r_3) with constraint $(r_1 \le r_2 \le r_3)$. Without loss of generality, we assume a lognormal model for r_3 and beta distribution for the two aspect ratios.

More specifically, we assume that $r_3 \sim \text{lognormal}(\mu, \sigma^2)$, $\frac{r_1}{r_2} \sim Beta(\alpha_1, \beta_1)$ and $\frac{r_2}{r_3} \sim Beta(\alpha_2, \beta_2)$, where r_3, $\frac{r_2}{r_3}$ and $\frac{r_1}{r_2}$ are independent and $\boldsymbol{\theta} = (\mu, \sigma^2, \alpha_1, \beta_1, \alpha_2, \beta_2)$ are the size distributional parameters to be estimated. The lognormal distribution is the most commonly used distribution in modeling particle sizes in geology, environmental science, material science, atmospheric sciences and aerobiology [21-23]. The beta distribution is very flexible in modeling distributions of different shapes defined on the interval [0,1]. For example, when $\alpha = \beta = 1$, the beta distribution degenerates to uniform distribution. If the two parameters are not equal, the distribution is either positively skewed or negatively skewed. The density function $f(r_1, r_2, r_3|\boldsymbol{\theta})$ can be obtained based on the variable transformation as

$$f(r_1, r_2, r_3|\boldsymbol{\theta}) = \text{logN}(r_3; \mu, \sigma^2) \prod_{i=1}^{2} \left(\frac{r_i}{r_{i+1}}\right)^{\alpha_i - 1} \left(1 - \frac{r_i}{r_{i+1}}\right)^{\beta_i} \frac{1}{r_{i+1} B(\alpha_i, \beta_i)} \tag{9}$$

As for the orientation angles p_i, we redefine p_i as the *absolute value* of the angle between the *i*-th semi-principal axis and XY plane for the sake of convenience, i.e, $p_i \in \left[0, \frac{\pi}{2}\right]$. The analytical form of $f(p_3)$ and $f(p_1|p_3)$ can be obtained based on Theorem 2 (see Appendix B for the proof).

Theorem 2: Under the Assumption (iii) in Section 2, the distribution of $\{p_i, i = 1,2,3\}$ has the following density functions:

$$f(p_i) = \cos p_i \,, p_i \in \left[0, \frac{\pi}{2}\right], i = 1,2,3 \tag{10}$$

$$f(p_i|p_j) = \frac{2}{\pi} \frac{\cos p_i}{\sin p_k}, (i, j, k) \in \text{Perm}(1,2,3) \tag{11}$$

where Perm (1,2,3) is the set of all permutations of indices {1,2,3} and $\sin p_k = \sqrt{1 - \sin^2 p_i - \sin^2 p_j}$.

The direct computation of the density function $f(d_1, d_2|\boldsymbol{h}, I = 1)$ is not applicable since the distribution of d_1 and d_2 is not available. However, the density function $f(z_c, p_1|\boldsymbol{h}, I = 1)$ could be directly calculated as

$$f(p_1, z_c|r_1, r_2, r_3, p_3, I = 1) = f(p_1|r_1, r_2, r_3, p_3, I = 1) f(\, z_c|r_1, r_2, r_3, p_3, p_1, I = 1) \tag{12}$$

where

$$f(p_1|r_1, r_2, r_3, p_3, I = 1) = f(p_1|p_3)\frac{z_u}{E(z_u|r_1, r_2, r_3, p_3)} \tag{13}$$

Under Assumption (i) in Section 2, given that an ellipsoid of semi-height z_u is intersected by an image plane, the center of that ellipsoid will be uniformly distributed in the proximity of the cutting plane of maximum distance z_u. Therefore the distance between the cutting plane and the center of the ellipsoid follows a uniform distribution with density function

$$f(\, z_c|r_1, r_2, r_3, p_3, p_1, I = 1) = \begin{cases} \frac{1}{z_u}, & 0 \le z_c \le z_u \\ 0, & \text{otherwise} \end{cases} \tag{14}$$

The density function $f(d_1, d_2|r_1, r_2, r_3, p_3, I = 1)$ can be computed based on the transformation of random variables

$$f(d_1, d_2|r_1, r_2, r_3, p_3, I = 1) = f(p_1(d_1, d_2), z_c(d_1, d_2)|r_1, r_2, r_3, p_3, I = 1)|J|^{-1} \tag{15}$$

Here p_1 and z_c are functions of r_1, r_2, r_3, p_3, d_1 and d_2, which can be computed based on Equation (1), and J is the Jacobian $J = \left|\frac{\partial(d_1, d_2)}{\partial(p_1, z_c)}\right|$ calculated as

$$J = \frac{2d_1 d_2 r_1^2 r_2^2 r_3^2 z_c}{(d_2^2 - d_1^2)C_1^3}[2C_1 C_2' - C_2 C_1'] \tag{16}$$

where $C_1 = \sum_{i=1}^{3} r_i^2 \sin^2 p_i$, $C_2 = \sum_{i=1}^{3} \frac{\cos^2 p_i}{r_i^2}$, $C_1' = (r_1^2 - r_2^2)\sin 2p_1$ and $C_2' = \left(\frac{1}{r_2^2} - \frac{1}{r_1^2}\right)\sin 2p_1$.

The computation of p_1 and z_c is given in Appendix C and the computation of J is given in Appendix D. Therefore, the complete-data likelihood function can be obtained by combining Equation (5-16) as

$$f(\boldsymbol{h}, d_1, d_2|\boldsymbol{\theta}, I = 1) = \frac{2}{\pi}\frac{\cos p_1 \cos p_3}{\sin p_2 \, E(z_u|\boldsymbol{\theta})}|J|^{-1} f(r_1, r_2, r_3|\boldsymbol{\theta}) \tag{17}$$

3.2.2 Quasi-Monte Carlo based EM Algorithm for Parameter Estimation

The EM algorithm is an iterative method to find the maximum of the likelihood function. There

are two steps in each iteration, namely, the expectation (E) step and the maximization (M) step. The E-step computes the expectation of the log-likelihood with respect to the conditional predictive density using the current estimate for the parameters. The M-step computes the parameters maximizing the expected log-likelihood obtained in the E-step. Denote $\boldsymbol{R} = (r_{i1}, r_{i2}, r_{i3}, i = 1, \dots, n)$, $\boldsymbol{P}_3 = \{p_{i3}, i = 1, \dots, n\}$, and $\boldsymbol{D} = (d_{i1}, d_{i2}, i = 1, \dots, n)$. The E-step and M-step can be mathematically formulated as

$$\text{E-step: } Q\left(\boldsymbol{\theta}, \widehat{\boldsymbol{\theta}}^{(k)}\right) = E_{\boldsymbol{R},\boldsymbol{P}_3|\widehat{\boldsymbol{\theta}}^{(k)},\boldsymbol{D}}(\log L(\boldsymbol{\theta}|\boldsymbol{D}, \boldsymbol{R}, \boldsymbol{P}_3)) \tag{18}$$

$$\text{M-step: } \widehat{\boldsymbol{\theta}}^{(k+1)} = \underset{\boldsymbol{\theta}}{\operatorname{argmax}}\left\{Q\left(\boldsymbol{\theta}, \widehat{\boldsymbol{\theta}}^{(k)}\right)\right\} \tag{19}$$

where $\widehat{\boldsymbol{\theta}}^{(k)}$ is the estimated parameters at iteration k. The likelihood $L(\boldsymbol{\theta}|\boldsymbol{D}, \boldsymbol{R}, \boldsymbol{P}_3)$ and the predictive density function $f(\boldsymbol{R}, \boldsymbol{P}_3|\widehat{\boldsymbol{\theta}}^{(k)}, \boldsymbol{D})$ can be expressed as

$$L(\boldsymbol{\theta}|\boldsymbol{D}, \boldsymbol{R}, \boldsymbol{P}_3) = \prod_{i=1}^{n} f(p_{i3}, r_{i1}, r_{i2}, r_{i3}, d_{i1}, d_{i2}|\boldsymbol{\theta}, I_i = 1) \tag{20}$$

$$f\left(\boldsymbol{R}, \boldsymbol{P}_3\middle|\widehat{\boldsymbol{\theta}}^{(k)}, \boldsymbol{D}\right) \propto \prod_{i=1}^{n} f\left(p_{i3}, r_{i1}, r_{i2}, r_{i3}, d_{i1}, d_{i2}|\widehat{\boldsymbol{\theta}}^{(k)}, I_i = 1\right) \tag{21}$$

where $f(p_{i3}, r_{i1}, r_{i2}, r_{i3}, d_{i1}, d_{i2}|\boldsymbol{\theta}, I_i = 1)$ is given in Equation (5) and (17).

However, in the E-step, the analytical form of the expectation $Q\left(\boldsymbol{\theta}, \widehat{\boldsymbol{\theta}}^{(k)}\right)$ is not tractable due to intractable predictive density function and high dimensional integrals. Monte Carlo sampling approach to approximate the expectation $Q\left(\boldsymbol{\theta}, \widehat{\boldsymbol{\theta}}^{(k)}\right)$is a natural way when the analytical form of the expectation is not tractable [24]. Specifically, at each iteration k, S samples $\boldsymbol{h}_i^{(k,s)} = \left(r_{i1}^{(k,s)}, r_{i2}^{(k,s)}, r_{i3}^{(k,s)}, p_{i3}^{(k,s)}\right), s = 1,2, \dots S$ can be sampled using the conditional predictive density $f(h_i|\widehat{\boldsymbol{\theta}}^{(k)}, d_{i1}, d_{i2}, I_{\mathrm{i}} = 1)$ for ellipsoids $i = 1,2, \dots, n$. To draw random samples, one might use the importance sampling or use the Markov Chain Monte Carlo (MCMC) approach such as the Metropolis-Hastings (MH) algorithm. For the importance sampling, the importance function can be simply selected as

$$g\left(h_i|\widehat{\boldsymbol{\theta}}^{(k)}\right) = f(p_{i3}) f\left(r_{i1}, r_{i2}, r_{i3}\middle|\widehat{\boldsymbol{\theta}}^{(k)}\right) \tag{22}$$

The unnormalized weight of each sample $\boldsymbol{h}_i^{(k,s)}$ among S samples for the ellipsoid i is easily calculated based on Equation (17) as

$$w_i^{*(k,s)} = \frac{2}{\pi}\frac{\cos p_{i1}^{(k,s)}}{\sin p_{i2}^{(k,s)}}\left|J^{(k,s)}\right|^{-1} \tag{23}$$

However, as observed in our research, both the importance sampling and the MH sampling based EM algorithms either fail to converge or result in inaccurate estimates, even if the sample size is significantly large. One main reason is that most of the generated samples are non-conforming, which means given the observed d_1 and d_2, there do not exist p_1 and z_c satisfying Equation (1) for many generated samples. A conforming sample (r_1, r_2, r_3, p_3) should satisfy the following constraints (see Appendix E for the derivation):

$$\begin{cases} r_3 \geq r_2 \geq r_1 \\ r_3 \geq \dfrac{d_2}{2} \\ r_2 \geq \max\left\{\dfrac{d_1}{2}, \sin p_3 \Big/ \sqrt{4/d_2^2 - \cos^2 p_3 / r_3^2}\right\} \\ r_1 \geq \sin p_3 \Big/ \sqrt{4/d_1^2 - \cos^2 p_3 / r_3^2} \end{cases} \tag{24}$$

A simple solution to avoid non-conforming samples and thus increase sampling efficiency is to sample p_3 from prior $f(p_3) = \cos p_3$ and sample (r_1, r_2, r_3) uniformly from space $\frac{d_2}{2} \leq r_3 \leq r_{max}, \frac{d_1}{2} \leq r_2 \leq r_3, 0 \leq r_1 \leq r_2$ or sample $(r_3, \frac{r_2}{r_3}, \frac{r_1}{r_2})$ uniformly from space $r_3 \in \left[\frac{d_2}{2}, r_{max}\right], \frac{r_2}{r_3} \in (0,1], \frac{r_1}{r_2} \in (0,1]$ where r_{max} is a pre-selected sufficiently large upper bound for r_3. However, in this method, the purely random draws do not explore the sample space well. Samples tend to form clusters, which may result in unexplored regions with no samples sitting in. As observed in our research, the EM algorithm tends to converge to inaccurate estimates of size parameters due to the persistent Monte Carlo errors.

To resolve this issue, we propose to use a Quasi-Monte Carlo (QMC) method [25]. QMC method produces a deterministic *low-discrepancy sequence* of points that are more uniformly distributed and can significantly improve the accuracy of Monte Carlo approximations of high-dimensional integrals over purely random sampling. The discrepancy measures the distribution deviation from uniformity for a sequence of points. There are a variety of low-discrepancy

sequences, including the Halton sequence [26], the Sobol sequence [27] etc. In this article, we select the Sobol sequence to sample $(\frac{r_3}{r_{max}}, \frac{r_2}{r_3}, \frac{r_1}{r_2})$. For p_3, we directly sample from its prior distribution. To reduce the computational load, a fixed set of samples with nonzero weight coefficients calculated by Equation (23) can be generated for each ellipsoid before the iteration of EM algorithm starts. The unnormalized weight of each sample $\boldsymbol{h}_i^{(s)} = \left(r_{i1}^{(s)}, r_{i2}^{(s)}, r_{i3}^{(s)}, p_{i3}^{(s)}\right)$ at iteration k can be calculated as

$$w_i^{(k,s)} = w_i^{*(s)} f\left(\frac{r_{i1}^{(s)}}{r_{i2}^{(s)}}, \frac{r_{i2}^{(s)}}{r_{i3}^{(s)}}, r_{i3}^{(s)} \middle| \widehat{\boldsymbol{\theta}}^{(k)}\right) \tag{25}$$

where $w_i^{*(s)}$ is the pre-calculated weight by Equation (23). Therefore at each iteration k the weights only need to be updated by multiplying $w_i^{*(s)}$ with $f\left(r_{i1}^{(s)}/r_{i2}^{(s)}, r_{i2}^{(s)}/r_{i3}^{(s)}, r_{i3}^{(s)} \middle| \widehat{\boldsymbol{\theta}}^{(k)}\right)$. Based on the weighted samples, the Q function $Q\left(\boldsymbol{\theta}, \widehat{\boldsymbol{\theta}}^{(k)}\right)$ is calculated as

$$Q\left(\boldsymbol{\theta} \middle| \widehat{\boldsymbol{\theta}}^{(k)}\right) = \sum_{i=1}^{n} \sum_{s=1}^{S} W_i^{(k,s)} \log f\left(r_{i1}^{(s)}, r_{i2}^{(s)}, r_{i3}^{(s)} \middle| \boldsymbol{\theta}\right) - n \log E(z_u|\theta) + C \tag{26}$$

where C is a constant independent of $\boldsymbol{\theta}$, and $W_i^{(k,s)}$ is the normalized weight calculated by

$$W_i^{(k,s)} = \frac{w_i^{(k,s)}}{\sum_{s=1}^{S} w_i^{(k,s)}} \tag{27}$$

In the M-step, Equation (26) needs to be maximized with respect to $\boldsymbol{\theta}$ to obtain $\widehat{\boldsymbol{\theta}}^{(k+1)}$ in the next iteration. However, due to the existence of the intractable term $\log E(z_u|\boldsymbol{\theta})$, the analytical solution is not tractable for all parameters. To address this issue, we propose to use the particle swarm optimization algorithm [28], where $\log E(z_u|\boldsymbol{\theta})$ is calculated through Monte Carlo simulation. Since

$$\log E(z_u|\boldsymbol{\theta}) = \left(\mu + \frac{\sigma^2}{2}\right) + \log E\left(\sqrt{\sin^2 p_3 + \left(\frac{r_2}{r_3}\right)^2 \sin^2 p_2 + \left(\frac{r_1}{r_2}\right)^2 \left(\frac{r_2}{r_3}\right)^2 (1 - \sin^2 p_3 - \sin^2 p_2)}\right),$$

we only need to sample $p_3, p_2, \frac{r_1}{r_2}, \frac{r_2}{r_3}$ to approximate $\log E(z_u|\boldsymbol{\theta})$. In summary, the proposed QMC based EM algorithm (QMC-EM) is given in Algorithm 1, where a stopping criterion

$\max_i \left|\left(\hat{\theta}_i^{(k)} - \hat{\theta}_i^{(k-1)}\right)/\hat{\theta}_i^{(k-1)}\right| < \delta$ is used to terminate the iterative algorithm.

Algorithm 1: QMC-EM Algorithm for Size Parameter Estimation

Initialize
  Generate Sobol samples
  For $i = 1{:}\, n$
    • Generate Sobol samples $\boldsymbol{h}_i^{(s)}$ until obtain S samples with nonzero weights $w_i^{*(s)}$
  End
  EM parameters: number of EM iteration *maxIter*
  Size parameters: $\widehat{\boldsymbol{\theta}}^{(0)}$
End
For $k = 1$:*maxIter*
  E-step
  For $i = 1{:}\, n$
    • Calculate $w_i^{(k,s)}$ and $W_i^{(k,s)}$ using Equation (25) and (27).
  End
  M-step
  Calculate $\widehat{\boldsymbol{\theta}}^{(k)}$ using the particle swarm optimization algorithm.
  If $\max_i \left|\frac{\hat{\theta}_i^{(k)} - \hat{\theta}_i^{(k-1)}}{\hat{\theta}_i^{(k-1)}}\right| < \delta$, stop
End

4. INFERRING THE DENSITY AND VOLUME FRACTION OF ELLIPSOID

In this section, we present the details of how to estimate the volume number density and volume fraction of ellipsoids. The linkage between the number density of particles in 2D and 3D space is established in Theorem 3 as follows.

Theorem 3: Under the Assumptions (i)-(iii) in Section 2, the particles shown on an image plane with area A can be modeled as an inhomogeneous Poisson process, and the number of particles on the image follows a Poisson distribution with parameter

$$\lambda = 2A\,\overline{z_u}\lambda_0 \tag{28}$$

where λ_0 is the density of particles in 3D space, $\overline{z_u}$ is the mean of z_u expressed as $\overline{z_u} = \int_0^{r_{max}} r f_{z_u}(r) dr$.

The detailed proof of Theorem 3 is given in Appendix F. We can see that the particles shown on the image follows the same Poisson distribution as the number of particles within the space swept

out by A along its normal vector delimited by $\pm\bar{z}_u$. Actually, the number of particles shown on the cutting image is just thinning a Poisson process. If we assume a sufficiently large upper bound r_{max} for the ellipsoid size r_3, then the number of particles within the swept-out space delimited by $\pm r_{max}$ follows the Poisson distribution with parameter $2Ar_{max}\lambda_0$. Denote this space as $S(r_{max})$. Since each particle is shown on the image with probability $\Pr(z_u \geq z_c)$, based on the thinning process, the number of particles shown on the image follows a Poisson distribution with parameter

$$\lambda = 2Ar_{max}\lambda_0 \Pr(z_u \geq z_c) = 2Ar_{max}\lambda_0 \int_0^{r_{max}} \frac{1}{r_{max}} \Pr(z_u \geq r)\, dr = 2A\,\overline{z_u}\lambda_0$$

Also, it can be easily shown that the particles not shown on the image within the space $S(r_{max})$ follows an independent Poisson distribution with parameter

$$\lambda' = 2A(r_{max} - \overline{z_u})\lambda_0 \tag{29}$$

The proof can be found in Resnick [29]. Note that in this paper we do not specify the upper bound for r_3 to reduce the number of parameters to estimate. Considering the micro-scaled size of particles (or images) and the macro-scaled specimen, the space on two sides of the cutting image can be modelled as an infinite space (thickness $\gg r$). In the Sobol sample generation, however, we can select a sufficiently large value r_{max} as the upper bound which satisfies $r_{max} > \max\{d_{i2}/2\}$.

Based on Equation (28), the particle density can be estimated using the observed number of particles n as

$$\hat{\lambda}_0 = \frac{n}{2A\overline{z_u}} \tag{30}$$

Given the n observed 2D ellipses on the intersectional image, the total number of ellipsoid in the space $S(r_{max})$ is $n + N'$ where $N' \sim \text{Poisson}(\lambda')$. Define ρ as the volume fraction of particles, then in the space $S(r_{max})$, ρ can be calculated as

$$\rho = \frac{\sum_{i=1}^{n} V_i + \sum_{j=1}^{N'} V_j'}{2Ar_{max}}$$

where V_i is the volume of the ith ellipsoid intersected by the cutting image and V_j' is the volume of uncross-sectioned particles. If the truncation upper bound r_{max} is sufficiently large or we consider the entire specimen which is significantly larger than $S(r_{max})$, then the observed number of

ellipses is negligible in the calculation of the distribution of total number of ellipsoids. In this article, we select the whole specimen as the 3D space to simplify the calculation. The mean and variance of ρ can be obtained through Theorem 4 as follows.

Theorem 4: Suppose the size of the ellipsoidal particles follows the distribution given in Equation (9). Under the Assumptions (i)-(iii) and given the particle density λ_0, the mean and variance of ρ are

$$\begin{aligned} E(\rho) &= \lambda_0 E(V_e) \\ Var(\rho) &= \frac{\lambda_0 E(V_e^2)}{V} \end{aligned} \tag{31}$$

where V is the volume of the specimen, V_e is the volume of an ellipsoid with $E(V_e)$ and $E(V_e^2)$ calculated as

$$E(V_e) = \frac{4\pi}{3}\frac{\alpha_1}{\alpha_1+\beta_1}\frac{\alpha_2\beta_2+\alpha_2^2(\alpha_2+\beta_2+1)}{(\alpha_2+\beta_2)^2(\alpha_2+\beta_2+1)}\exp(3\mu+\frac{9}{2}\sigma^2)$$

$$E(V_e^2) = \frac{32\pi^2}{3}\frac{\alpha_1\beta_1+\alpha_1^2(\alpha_1+\beta_1+1)}{(\alpha_1+\beta_1)^2(\alpha_1+\beta_1+1)}\frac{[\alpha_2^3+\alpha_2^2(1-2\beta_2)+\beta_2^2(1+\beta_2)-2\alpha_2\beta_2(2+\beta_2)]}{\alpha_2\beta_2(\alpha_2+\beta_2+2)(\alpha_2+\beta_2+3)}\exp(6\mu+18\sigma^2)$$

The proof of this theorem can be found in Appendix G. Equation (31) indicates that to obtain an accurate estimate of the mean and variance of ρ, it is essential to get an accurate inference of λ_0 based on Equation (30). Since $\hat{\lambda}_0$ is an unbiased estimator of λ_0, the variance of $\hat{\lambda}_0$ should be sufficiently small to achieve a desired estimation accuracy. Based on Equation (28) and (30), the estimation variance of the normalized parameter $\hat{\lambda}_0/\lambda_0$ can be calculated as

$$Var\left(\frac{\hat{\lambda}_0}{\lambda_0}\right) = \frac{1}{\lambda_0^2}\frac{\lambda}{(2A\overline{z_u})^2} = \frac{1}{2A\lambda_0\overline{z_u}} = \frac{1}{\lambda} \tag{32}$$

From the above equation we can see that the percentage error of the estimation mainly depends on λ, i.e., the Poisson parameter of the particles shown on cross-sectional images. Therefore in applications, the estimation accuracy of both size parameters and particle density only depend on the total number of observed particles. In other words, if the particle density is large, a relatively small number of images or an image with small area is sufficient. While if the observed 2D density is very small, a large image is required. As for the volume fraction ρ, since the volume of the

specimen is often significantly larger than $\lambda_0 E(V_e^2)$, i.e., $V \gg \lambda_0 E(V_e^2)$, ρ can be approximately treated as a deterministic quantity.

In practice, the volume fraction is often alternatively estimated using the area fraction of ellipses in the cross-sectional images [4]. Here we provide a justification of this method by proving that the expectation of the volume fraction is actually identical to that of the area fraction, which is given in Theorem 5.

Theorem 5: Let A_v denote the total cross-sectional area of the intersected ellipsoids on the cutting image of area A. Under Assumptions (i) and (ii), we have

$$E(\rho) = E\left(\frac{A_v}{A}\right) \tag{33}$$

The proof is given in Appendix H. Theorem 5 indicates that the mean volume fraction can be unbiasedly estimated by simply calculating the area fraction of ellipses. From Appendix H we can see that the ellipsoids do not need to be uniformly oriented. Besides, we can easily prove that Equation (33) is still true for spherical particles. Therefore, to estimate the mean volume fraction, Equation (33) is simpler and much more flexible than Equation (31).

5. SIMULATION STUDY

In this section we use the Monte Carlo simulations to verify the theoretical results and evaluate the effectiveness of the established approach. In Section 5.1 we investigate the estimation of size parameters with different numbers of cross-sectional ellipses. In Section 5.2 we study the joint estimation of the size distribution, particle number density and volume fraction.

5.1 Size Parameter Estimation

In the simulation study, the size distribution parameters are set to be $\mu = -3.5$, $\sigma^2 = 0.5$, $\alpha_1 = 15$, $\beta_1 = 3$, $\alpha_2 = 20$, $\beta_2 = 6$. To simulate the elliptical cross sections of a fixed sample size n, the following steps are employed: (1) simulate a large number of samples from the distribution $f(r_1, r_2, r_3, p_3, p_2|\boldsymbol{\theta})$; (2) calculate the weight z_u of each sample; (3) draw n samples from the generated samples through weighted sampling with z_u as the weight; (4) simulate z_c based on Equation (14) for the n selected samples. The procedure to simulate the orientation angles p_i in the first step is provided in Appendix I. In the QMC-EM algorithm, the QMC sample size is set to

$S = 1 \times 10^6$. The stopping criterion threshold is set to $\delta = 0.015$. To reduce the total number of iterations for convergence, the initial values are set as follows: μ and σ^2 are obtained by fitting a lognormal distribution using the n observed d_2; α_2 and β_2 are obtained by fitting a beta distribution using the observed d_1/d_2; α_1 and β_1 are arbitrarily set as 1.

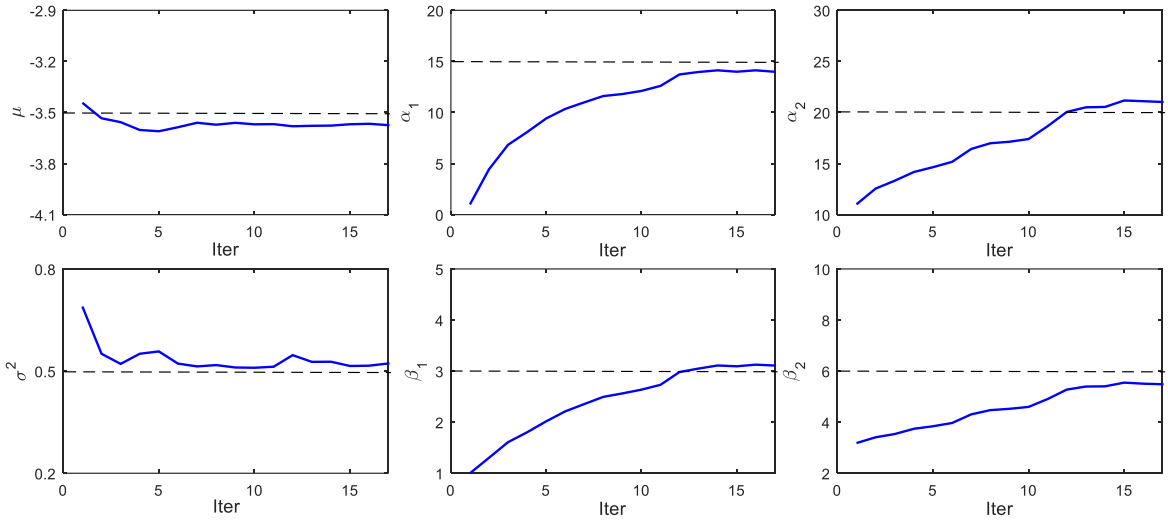

Figure 5. Convergence of the QMC-EM algorithm for one run with $n = 600$. The horizontal dashed lines denote the true values.

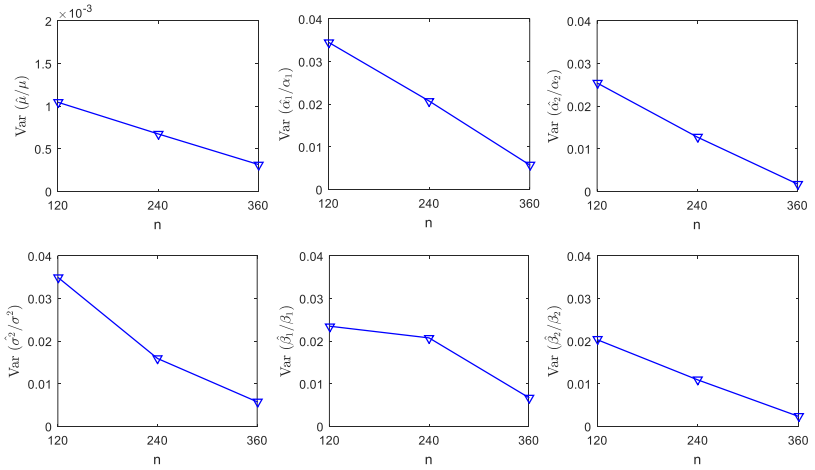

Figure 6. The estimation variance of the normalized parameters with different sample sizes n

Figure 5 illustrates the convergence of the QMC-EM algorithm for one simulation run with $n = 600$. As we can see, with only about 13 iterations, all the parameters converge rapidly from the initial values to those very close to the true ones. The computational time of each iteration of the EM algorithm for $n = 600$ ellipses is about 20 minutes using MATLAB running on a Windows

Server 2012 with Intel Xeon Processor E5-2650 and 20 cores. Figure 6 shows the estimation variance of the normalized parameters with different sample sizes. As expected, the estimation variance decreases as n increases. Note that due to the inherent Monte Carlo errors at both the E-step and M-step, the estimation variance will eventually converge to a nonzero value as n continues to increase.

5.2 Joint Estimation of Size Distribution, Number Density and Volume Fraction

In this section, we simulate multiple microscopic images of different sizes to jointly estimate the size distribution, number density and volume fraction. The size distributional parameters are set the same as used in Sec. 5.1. The particles follow a Poisson distribution with density parameter $\lambda_0 = 6.3492/\text{mm}^3$. The Poisson parameter for the intersected particles is $\lambda = 0.4A$. Three image sizes are selected: $A = 300, 600$ and $900\ \text{mm}^2$. For each simulation setting, the simulation is replicated 20 times. The QMC-EM algorithm parameters are the same as in Section 5.1.

Table 1. Summary of the size distribution, number density and volume fraction estimation

A	n	$\hat{\mu}$	$\widehat{\sigma^2}$	$\hat{\alpha}_1$	$\hat{\beta}_1$	$\hat{\alpha}_2$	$\hat{\beta}_2$	$\widehat{\bar{z}_u}$	$\widehat{\bar{V}_e}(10^{-4})$	$\hat{\lambda}_0$	CI	$\hat{\rho}$ (%)	$\frac{A_v}{A}$ (%)
	104	-3.46	0.520	12.6	2.91	15.0	4.78	0.0328	6.454	5.29	[4.27, 6.30]	0.341	0.292
	117	-3.72	0.637	11.3	2.04	13.1	3.81	0.0271	5.293	7.20	[5.90, 8.50]	0.381	0.416
300	118	-3.49	0.492	15.5	2.77	20.6	6.05	0.0319	5.581	6.16	[5.05, 7.27]	0.344	0.386
	128	-3.38	0.411	15.2	2.85	17.9	5.32	0.0340	5.287	6.27	[5.19, 7.36]	0.332	0.320
	121	-3.59	0.492	12.2	2.52	19.4	5.64	0.0289	4.105	6.98	[5.74, 8.22]	0.287	0.287
	246	-3.65	0.646	15.7	3.34	20.8	6.36	0.0291	6.658	7.03	[6.15, 7.91]	0.468	0.463
	223	-3.57	0.516	16.7	3.49	23.8	7.16	0.0296	4.731	6.28	[5.45, 7.10]	0.297	0.282
600	238	-3.46	0.459	15.6	3.07	21.3	6.45	0.0321	5.100	6.18	[5.39, 6.96]	0.315	0.320
	268	-3.55	0.497	15.5	3.18	22.7	6.82	0.0298	4.565	7.49	[6.59, 8.39]	0.342	0.333
	231	-3.45	0.498	16.9	3.62	20.8	6.32	0.0330	6.231	5.82	[5.07, 6.58]	0.363	0.350
	360	-3.51	0.518	15.4	3.02	19.1	5.65	0.0317	5.876	6.31	[5.66, 6.96]	0.371	0.360
	338	-3.54	0.526	15.5	3.39	19.86	6.14	0.0304	5.261	6.19	[5.52, 6.83]	0.325	0.343
900	348	-3.47	0.493	16.29	3.36	21.3	6.29	0.0322	5.705	6.00	[5.37, 6.63]	0.342	0.375
	363	-3.55	0.557	15.3	3.03	20.6	6.14	0.0307	5.996	6.57	[5.89, 7.25]	0.394	0.344
	367	-3.45	0.483	14.3	3.20	20.8	5.69	0.0331	6.012	6.16	[5.53, 6.79]	0.370	0.371
True		-3.5	0.5	15	3	20	6	0.0315	5.456	6.35		0.346	0.346

Table 1 shows the detailed estimation results of the first 5 replications for each image size A, where n is the number of particles shown on the image, $\widehat{\bar{z}_u}$ and $\widehat{\bar{V}_e}$ are the estimated mean of z_u and V_e

respectively, CI is the 95% confidence interval of the estimator $\hat{\lambda}_0$, $\hat{\rho}$ and A_v/A are the estimated volume fractions using Equation (31) and (33) respectively. The bottom row provides the true values of the parameters. Table 2 shows the standard error of the estimation of the normalized parameters, i.e., $\sqrt{\frac{1}{r}\sum_{i=1}^{r}\left(\frac{\hat{p}_i-p}{p}\right)^2}$ where $r = 20$ is the number of replications and p is the parameter to estimate. Clearly, the estimation accuracy of all these parameters increases as the image size increases. Among these six distribution parameters, the mean parameter μ has the lowest estimation error. It may be explained in terms of MLE bias and information inequality. It can be easily shown that the MLE of μ is unbiased while the MLEs of the other five parameters are biased. Besides, based on the Cramer-Rao inequality [30], the estimation variance of μ has lower bound than other parameters, which is consistent with the results in Figure 6 that the estimation variance of μ is much smaller than other parameters. Comparing these two volume fraction estimation methods, we see that the estimated volume fractions in each run are very close to each other. Consequently, the overall estimation accuracies for these two methods are comparable, as shown in Table 2. For $A = 300$ and 600, the first method is slightly more accurate than the area fraction method. When the image size increases to 900, however, the area fraction method turns out to be more accurate, though the difference is not significant. The reason may be that for small sample sizes, the first method utilizes more information for volume fraction inference, and thus provide a more accurate estimation; while for large sample sizes, the estimation accuracy for the first method is limited or influenced by the inherent error of QMC-EM algorithm.

Table 2. Standard estimation error of the normalized parameters

A	$\hat{\mu}$	$\widehat{\sigma^2}$	$\hat{\alpha}_1$	$\hat{\beta}_1$	$\hat{\alpha}_2$	$\hat{\beta}_2$	$\widehat{\bar{z}_u}$	$\widehat{\bar{V}_e}$	$\hat{\lambda}_0$	$\hat{\rho}$	A_v/A
300	0.033	0.183	0.185	0.148	0.154	0.141	0.073	0.142	0.14	0.223	0.245
600	0.026	0.123	0.141	0.146	0.111	0.104	0.069	0.146	0.124	0.168	0.187
900	0.019	0.076	0.086	0.080	0.042	0.047	0.057	0.121	0.088	0.120	0.118

We also compared the proposed method with the one assuming all particles are spherical. In the sphere model, the observed radii are approximated by the geometric mean of the semi-major and semi-minor axes, i.e., $\sqrt{d_1 d_2}/2$. A log-normal distribution is also assumed for the radius of spherical particles. Table 3 shows the mean of the estimated parameters in 20 replications with $A =$

900. Clearly, the semi-major axes have been significantly underestimated under the spherical-particle assumption, which consequently leads to an underestimated mean semi-height $\bar{z}_u$ and mean particle volume $\overline{V_e}$. The number density λ_0 is significantly overestimated, which is what we expect based on Equation (30). The volume fraction ρ which is estimated by $\lambda_0\overline{V_e}$ is overestimated due to the dominant influence of the number density λ_0. Note that in this case study the means of the ratios r_2/r_3 and r_1/r_2 are about 0.77 and 0.83 respectively, which are close to 1. If we reduce these ratios, the inaccuracy of parameter estimation using spherical-model will become more significant.

Table 3. Comparison of parameter estimation using ellipsoid and sphere model

Model	$\hat{\mu}$	$\widehat{\sigma^2}$	$\widehat{\bar{z}_u}$	$\widehat{\overline{V_e}}(10^{-4})$	$\hat{\lambda}_0$	$\hat{\rho}(\%)$
Ellipsoid	-3.51	0.51	0.0308	5.382	6.40	0.344
Sphere	-3.80	0.54	0.0294	5.308	6.87	0.365
True Value	-3.50	0.50	0.0315	5.456	6.35	0.346

6. Application to Porosity Inference in Additive Manufacturing

In this section, the proposed method is applied to estimate the size distribution, volume number density and porosity in the metal additive manufacturing based on cross-sectional images. Metal-based additive manufacturing, such as Selective Laser Melting (SLM) and Electron Beam Melting (EBM), utilizes high energy density electron or laser beam as the energy source in the fabrication process. Porosity is one of the most severe quality issues that poses a significant challenge for wide adoption of metal-based AM process. The formation mechanisms of pores in metallic AM processes have been intensively studied through both experiment and simulation [31-35]. It has been widely agreed that the pore formation is related to the global energy density $E = P/(v_s\delta_l h_d)$, where P is the beam power, v_s is the scanning velocity, h_d is the hatch distance and δ_l is the layer thickness. At the region $E < E_{opt}$ where E_{opt} is the optimal energy density, porosity decreases as we increase E. In this region, the porosity is mainly due to the lack of fusion of powder particles caused by incomplete melting of the raw powders, balling effect and hillocks [33]. In these cases, formed pores are of complex, elongated shapes with sharp and concave boundaries. On the other hand, excessive energy density, i.e., $E > E_{opt}$, causes vaporization of the material, thus

producing spherical or near-spherical pores due to gas bubble formation. Increasing the energy density in this region will cause higher porosity.

Porosity is greatly affected by process parameters. Therefore, it is important to characterize it for quality inspection and process optimization. Currently, the most commonly used inspection methods include (1) the measurement of volume and mass with known full-dense density [1]; (2) the Archimedes method [1]; (3) wave speed measurement [36] and (4) X-ray computed tomography (X-Ray CT) [4, 37]. However, the first three methods only provide the overall volume fraction of defects in the final product. The void morphology, size and volume density, which are critical to the mechanical properties of the final product, are not available. X-Ray CT is capable of reconstructing 3D voids based on X-ray cross-sectional images or slices. However, this technique is seriously limited by its resolution [38]. It is not able to detect voids within an order of micrometers. Consequently, it is desirable to develop microscopic image based porosity inference technique.

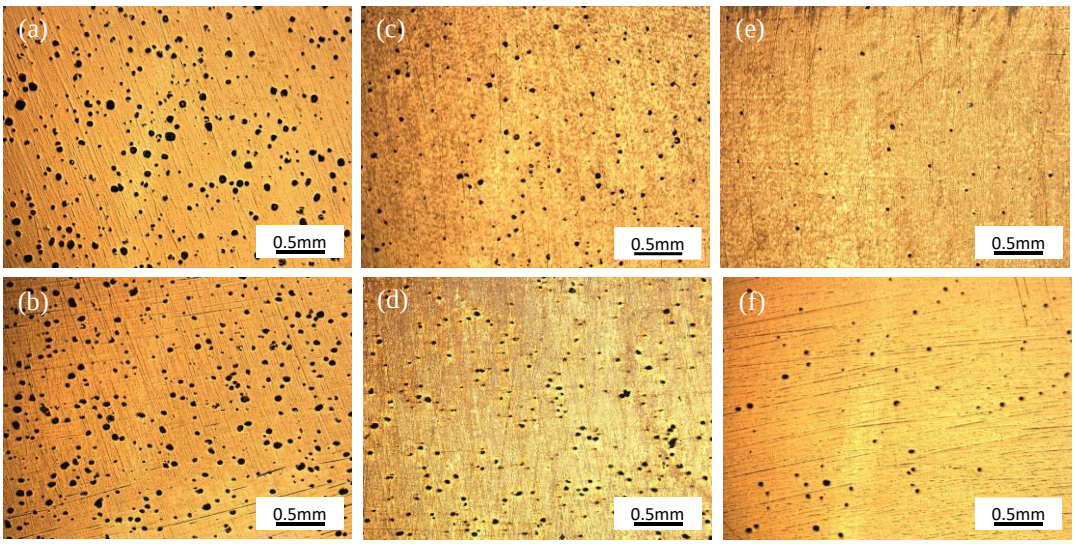

Figure 7. The cross-sectional images of SLM-produced Ti-6Al-4V specimens with laser power 120W and scan speed: (a-b) 360mm/s, (c-d) 480mm/s and (e-f) 600mm/s.

In this case study, we only consider the second AM process condition $E > E_{opt}$, where the pores are caused by gas bubbles with spherical or ellipsoidal shapes and uniform distribution in the specimen. The formed pores in the first case, i.e., $E < E_{opt}$ do not satisfy our model assumptions and thus are not considered. Figure 7 shows the cross-sectional images of three SLM-produced Ti-6Al-4V specimens with laser power 120 W and scan speed of 360, 480 and 600 mm/s

respectively [4]. For each specimen, microscopic images of size 3.6 mm × 2.7 mm (1920 pixel × 2560 pixel) are obtained at different locations. We can clearly see that increasing the scan speed decreases porosity within the speed range [360mm/s, 600mm/s] due to the reduction of global energy density. Besides, the circularity and elongation distribution of these voids indicate that most defects have an elliptical contour [4]. To analyze the porous defects, raw images are first converted to binary images, and then the boundaries or contours of defects are extracted, as shown in Figure 8. The boundaries of voids are then fitted to ellipses using nonlinear least square method, i.e., minimizing the sum of squared distances from the extracted data points to the ellipse boundary.

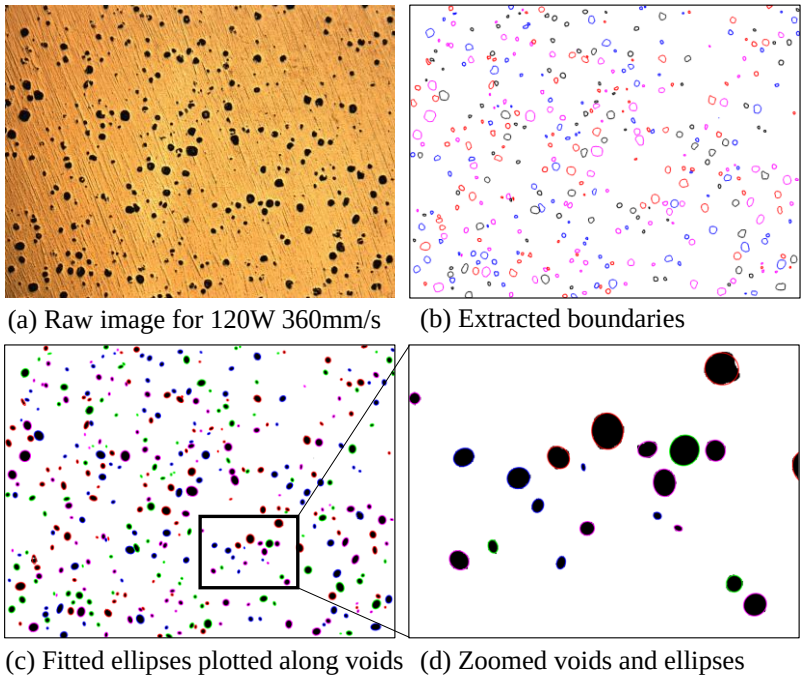

Figure 8. The segmentation and ellipsoidal fitting of porous defects from cross-sectional images

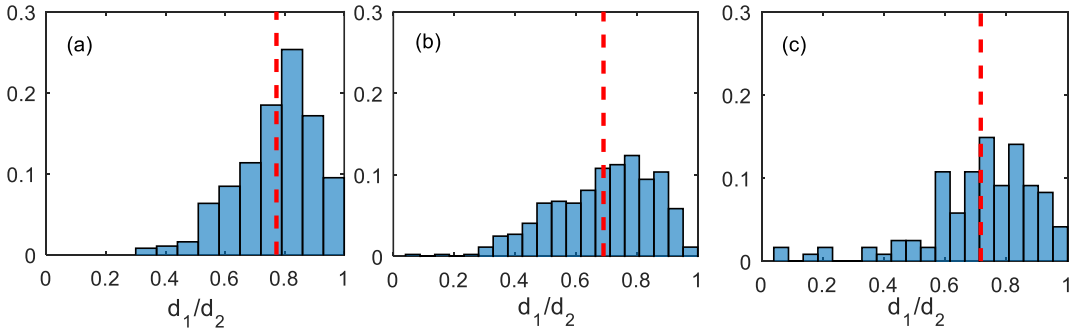

Figure 9. Histogram of aspect ratios d_1/d_2 for three specimens: (a) 360mm/s; (b) 480mm/s and (c) 600 mm/s. The vertical dashed lines denote the mean values.

For the first specimen, one cross-sectional image (Figure 7a) is used for porosity inference. For

the other two specimens, two and four cross-sectional images are used respectively due to low void densities. Figure 9 shows the aspect ratios d_1/d_2 of the fitted ellipses with mean values of 0.77, 0.69, and 0.72 respectively for the three specimens. Clearly, the deviation of the aspect ratio from utility indicates that ellipse is better than circle to capture the boundaries of void cross-sections. To validate the assumption of complete spatial randomness (CSR), we utilize Ripley's K function [39], which is defined as

$$K(t) = E(\text{num of voids within distance } t \text{ of a randomly chosen void})/\lambda$$

Under CSR, $K(t) = \pi t^2$. Therefore, we can test the difference between the theoretically calculated $K(t)$ curve under CSR and the estimated $\widehat{K}$ based on the observations. In practice, it is better to use the L function $L(t) = \sqrt{K(t)/\pi}$ since the estimated $\hat{L}(t)$ has an approximately constant variance. Under CSR, $L(t) = t$. To test if $L(t) = t$, we use the test statistic $\hat{L}_s = \sum_t |\hat{L}(t) - t|$. The p-values for the hypothesis testing are obtained through Monte Carlo simulations. Figure 10 shows the theoretical K function under CSR, the estimated $\widehat{K}$, the histograms of the simulated $\hat{L}_s$ and observed test statistics for the three specimens. We can clearly see that the estimated $\widehat{K}$ function is very close to the theoretical K function. The p-values of the hypothesis testing are 0.466, 0.757 and 0.596 respectively for the three specimens, all of which are not significant. Therefore, it is reasonable to assume all the voids are uniformly distributed.

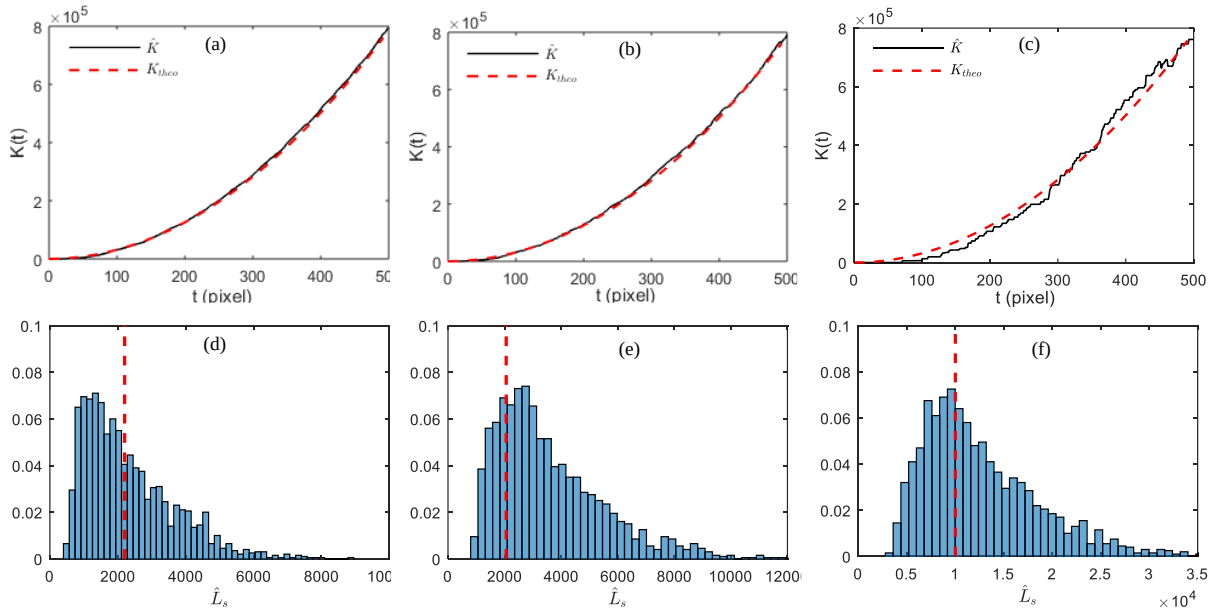

Figure 10. CSR test using Ripley's K function. (a, b, c): the estimated and theoretical K functions for the three specimens; (d, e, f): histograms of the Monte Carlo simulated $\hat{L}_s$ and observed $\hat{L}_s$

statistic denoted by vertical dashed lines. (a, d): 360mm/s, (b, e): 480mm/s and (c, f): 600m/s.

Table 4 shows the estimated size distribution parameters and volume number densities for the three specimens using the developed QMC-EM algorithm. As we can see, increasing the scanning speed or consequently decreasing the energy density E, both the size and volume number density decrease, which is consistent with the pore formation mechanism that decreasing the energy density E in the region $E > E_{opt}$ will reduce the porosity due to reduction of the vaporization.

Table 4. The distribution size and volume number density estimation

S	$A_i(\mathrm{mm}^2)$	n	$\hat{\mu}$	$\widehat{\sigma^2}$	$\hat{\alpha}_1$	$\hat{\beta}_1$	$\hat{\alpha}_2$	$\hat{\beta}_2$	$\widehat{\bar{z}_u}$	$\widehat{\bar{V}_e}(10^{-5})$	$\hat{\lambda}_0$	$CI(95\%)$
1	9.72	379	-3.697	0.121	6.31	1.65	9.39	2.10	0.022	5.93	889.6	[800.1, 979.2]
2	19.44	445	-3.700	0.053	4.63	2.14	10.43	2.99	0.020	3.38	572.9	[519.7, 626.1]
3	38.88	241	-3.899	0.070	2.41	0.90	10.68	2.75	0.017	2.24	182.8	[159.7, 205.9]

Table 5 shows the comparison of the size parameter estimation using ellipsoid and sphere models. Similar to the simulation study, the sphere model underestimated the semi-height $\bar{z}_u$ and overestimated the volume number density λ_0 for all three specimens compared with the ellipsoid model. However, the estimated mean volume $\bar{V}_e$ by the sphere model is larger than that of the ellipsoid model.

Table 5. Comparison of size parameter estimation using ellipsoid and sphere models

S	$\hat{\mu}$		$\widehat{\sigma^2}$		$\hat{\lambda}_0$		$\widehat{\bar{z}_u}$		$\widehat{\bar{V}_e}(10^{-5})$	
	Sphere	Ellipsoid	Sphere	Ellipsoid	Sphere	Ellipsoid	Sphere	Ellipsoid	Sphere	Ellipsoid
1	-3.943	-3.697	0.171	0.121	923.3	889.6	0.021	0.022	6.58	5.93
2	-4.060	-3.700	0.102	0.053	635.0	572.6	0.018	0.020	3.40	3.38
3	-4.245	-3.899	0.089	0.070	207.7	182.8	0.015	0.017	1.84	2.24

Table 6 shows the porosity (volume fraction) estimation using the proposed method and other four methods, e.g., the sphere model based method, area fraction of 2D voids, the Archimedes method, and the X-Ray CT method. The Archimedes method directly determines the density of the specimens by measuring the mass in air and water. Therefore it can be considered as a benchmark to evaluate the accuracy of other methods. The X-Ray CT method estimates the porosity by calculating the area fraction of voids on X-Ray slices. Clearly, the X-Ray CT method has the lowest accuracy for all three specimens than all other methods. It significantly underestimates the

porosity, especially for the second and third specimens with small pores, due to its incapability of detecting small voids. The area fraction method has higher accuracy on the first and third specimens while lower on the second specimen than the proposed ellipsoid model and sphere model based methods. Comparing the ellipsoid model with the sphere model, the former is better on the second and third specimen while worse on the first specimen than the latter. The reason may be that the second and third specimens have smaller aspect ratios d_1/d_2 (0.69 and 0.72) than the first specimen (0.77). The smaller the aspect ratio, the better the ellipsoid model than the sphere model.

Table 6. Comparison of porosity estimation using different methods

Specimen	Ellipsoid	Sphere	Area Fraction	X-Ray CT	Archimedes
1	5.27%	6.08%	6.01%	6.63%	5.85%
2	1.93%	2.16%	1.34%	1.03%	1.99%
3	0.41%	0.38%	0.47%	0.22%	0.46%

7. CONCLUSION AND DISCUSSION

In this paper, we proposed a series of statistical approaches to inferring 3D ellipsoidal particles based on cross-sectional images, including the size distribution, particle volume number density and volume fraction. The particles are modelled as ellipsoids, and the linkage between 3D ellipsoids and 2D cross-sectional contours on size and geometry is established. The likelihood function is derived and an efficient Quasi-Monte Carlo EM algorithm is developed to estimate the size distribution of ellipsoidal particles in specimens. The linkage between 3D and 2D particle number density is also established for density estimation. Specifically, we proved that particles shown on cross-sectional images can be modelled by a nonhomogeneous Poisson process. The volume fraction of 3D particles can be estimated based on the size and density estimations. We also provided a theoretical foundation for the area fraction estimation method by proving that the area fraction is an unbiased estimation of the mean of the porosity. Both the simulation and case studies show that the proposed method can effectively infer 3D ellipsoidal particles based on 2D cross-sectional images. It is worth noting that the proposed method is destructive in that the specimen needs to be cut for SEM image preparation. Its main application is in the fabrication process design and optimization stage, not the in-line quality inspection stage.

There are still some open issues worth of investigation in 3D particle inference. First of all, in the proposed method, orientations of ellipsoids are assumed to be uniformly distributed. However, this might not always be the case in practice. Due to many known or unknown factors, the orientation or the longest principal axis may favor certain directions. In such situation, inferring size distribution, particle density, orientation and volume fraction is very challenging. In addition, the assumption of uniform distribution is an ideal case where the fabrication process is perfectly stable. In practice, however, there may exist spatial clustering where the particles/pores may be denser in certain region than others due to unstable process conditions. The third issue that needs to be investigated is the selection of appropriate distributions for sizes of ellipsoids. Although lognormal and beta distributions are very flexible in characterizing size distributions, they may not be the best option. These open issues are left for our future work.

APPENDIX A: PROOF OF THEOREM 1

(1) The ellipsoid defined by $\{r_i, \theta_i, p_i, i = 1,2,3\}$ can be obtained by rotating a standard ellipsoid centered at the origin with three semi-principal axes r_1, r_2 and r_3 aligned with x, y and z axes, respectively. It is straightforward to obtain the rotation transformation matrix R as

$$R = \begin{bmatrix} \cos\theta_1 \cos p_1 & \cos\theta_2 \cos p_2 & \cos\theta_3 \cos p_3 \\ \sin\theta_1 \cos p_1 & \sin\theta_2 \cos p_2 & \sin\theta_3 \cos p_3 \\ \sin p_1 & \sin p_2 & \sin p_3 \end{bmatrix} \quad \text{(A. 1)}$$

The analytical equation for the ellipsoid can be expressed as

$$(x, y, z)RDR'(x, y, z)' = 1$$

where D $= \text{diag}(\frac{1}{r_1^2}, \frac{1}{r_2^2}, \frac{1}{r_3^2})$. Define A, A_{11}, A_{21}, A_{12} and A_{22} as

$$A = RDR' = \begin{bmatrix} a_{11} & a_{12} & a_{13} \\ a_{21} & a_{22} & a_{23} \\ a_{31} & a_{32} & a_{33} \end{bmatrix} = \begin{bmatrix} A_{11} & A_{12} \\ A_{21} & A_{22} \end{bmatrix} \quad \text{(A. 2)}$$

where $A_{11} = \begin{bmatrix} a_{11} & a_{12} \\ a_{21} & a_{22} \end{bmatrix}$, $A_{21} = A_{12}' = (a_{31}, a_{32})$ and $A_{22} = a_{33}$.

Suppose the ellipsoid is cut with a horizontal plane at the location $z = z_c$. Then the cross section can be expressed by

$$(x, y, z_c)RDR'(x, y, z_c)' = 1$$

$$\left[\begin{pmatrix} x \\ y \end{pmatrix} + z_c A_{11}^{-1} A_{12}\right]' A_{11} \left[\begin{pmatrix} x \\ y \end{pmatrix} + z_c A_{11}^{-1} A_{12}\right] = 1 - z_c^2 (A_{22} - A_{21} A_{11}^{-1} A_{12}) \quad \text{(A. 3)}$$

Since A is a symmetric and positive definite matrix, A_{11} is also a symmetric and positive definite matrix. Therefore (A. 3) is the equation of an ellipse. In other words, the intersection is an ellipse. The center is located at $(x_0, y_0)' = -z_c A_{11}^{-1} A_{12}$.

(2) The size of the ellipse is derived as follows.

Based on Eq. (A. 1) and (A. 2), A_{11} can be calculated as

$$a_{11} = \frac{(\cos\theta_1 \cos p_1)^2}{r_1^2} + \frac{(\cos\theta_2 \cos p_2)^2}{r_2^2} + \frac{(\cos\theta_3 \cos p_3)^2}{r_3^3}$$

$$a_{21} = a_{12} = \frac{\sin\theta_1 \cos\theta_1 (\cos p_1)^2}{r_1^2} + \frac{\sin\theta_2 \cos\theta_2 (\cos p_2)^2}{r_2^2} + \frac{\sin\theta_3 \cos\theta_3 (\cos p_3)^2}{r_3^2}$$

$$a_{22} = \frac{(\sin\theta_1 \cos p_1)^2}{r_1^2} + \frac{(\sin\theta_2 \cos p_2)^2}{r_2^2} + \frac{(\sin\theta_3 \cos p_3)^2}{r_3^2}$$

Since R is an orthogonal matrix and three semi-principal axes follow right-hand rule, then

$$\frac{\sin p_i \sin p_j}{\cos p_i \cos p_j} + \cos(\theta_j - \theta_i) = 0 \text{ for any } i \neq j \text{ (Orthogonal)} \quad \text{(A. 4)}$$

$$\begin{cases} \sin p_1 = \cos p_2 \cos p_3 \sin(\theta_3 - \theta_2) \\ \sin p_2 = \cos p_3 \cos p_1 \sin(\theta_1 - \theta_3) \text{ (right-hand rule)} \\ \sin p_3 = \cos p_1 \cos p_2 \sin(\theta_2 - \theta_1) \end{cases} \quad \text{(A. 5)}$$

$$\sin^2 p_1 + \sin^2 p_2 + \sin^2 p_3 = 1 \text{ (unit row vector)} \quad \text{(A. 6)}$$

Based on (A. 4), (A. 5) and (A. 6) we can calculate the determinant $|\mathrm{A}_{11}|$ as

$$|\mathrm{A}_{11}| = \frac{\sin^2 p_3}{r_1^2 r_2^2} + \frac{\sin^2 p_2}{r_1^2 r_3^2} + \frac{\sin^2 p_1}{r_2^2 r_3^2} \quad \text{(A. 7)}$$

A_{21} and A_{22} are calculated as

$$A_{21}(1) = a_{31} = \frac{\cos\theta_1 \sin p_1 \cos p_1}{r_1^2} + \frac{\cos\theta_2 \sin p_2 \cos p_2}{r_2^2} + \frac{\cos\theta_3 \sin p_3 \cos p_3}{r_3^2}$$

$$A_{21}(2) = a_{32} = \frac{\sin\theta_1 \sin p_1 \cos p_1}{r_1^2} + \frac{\sin\theta_2 \sin p_2 \cos p_2}{r_2^2} + \frac{\sin\theta_3 \sin p_3 \cos p_3}{r_3^2}$$

$$A_{22} = a_{33} = \frac{\sin^2 p_1}{r_1^2} + \frac{\sin^2 p_2}{r_2^2} + \frac{\sin^2 p_3}{r_3^2}$$

$|A_{11}|A_{21}A_{11}^{-1}A_{12}$ is calculated as

$$\begin{aligned} &|A_{11}|A_{21}A_{11}^{-1}A_{12} \\ &= \frac{r_1^2 \sin^2 p_2 \sin^2 p_3 + r_2^2 \sin^2 p_1 \sin^2 p_3}{r_1^4 r_2^4} + \frac{r_1^2 \sin^2 p_2 \sin^2 p_3 + r_3^2 \sin^2 p_1 \sin^2 p_2}{r_1^4 r_3^4} \\ &+ \frac{r_2^2 \sin^2 p_1 \sin^2 p_3 + r_3^2 \sin^2 p_1 \sin^2 p_2}{r_2^4 r_3^4} \\ &- 2\left[\frac{\sin^2 p_1 \sin^2 p_2 + \sin^2 p_1 \sin^2 p_3 + \sin^2 p_2 \sin^2 p_3}{r_1^2 r_2^2 r_3^2}\right] \end{aligned}$$

Define $I = \{(1,2,3), (2,3,1), (3,1,2)\}$, then

$$1 - z_c^2 (A_{22} - A_{21} A_{11}^{-1} A_{12}) =$$

$$= 1 - z_c^2 \left(\sum_{i=1}^{3} \frac{\sin^2 p_i}{r_i^2} - \frac{1}{\sum_{(i,j,k)\in I} \frac{\sin^2 p_k}{r_i^2 r_j^2}} \left[\sum_{(i,j,k)\in I} \frac{\sin^2 p_k \, (r_i^2 \sin^2 p_j + r_j^2 \sin^2 p_i)}{r_i^4 r_j^4} - 2 \frac{\sum_{(i,j,k)\in I} \sin^2 p_i \sin^2 p_j}{r_1^2 r_2^2 r_3^2} \right] \right)$$

$$= 1 - \frac{z_c^2}{r_1^2 \sin^2 p_1 + r_2^2 \sin^2 p_2 + r_3^2 \sin^2 p_3}$$

Therefore

$$\left[\begin{pmatrix} x \\ y \end{pmatrix} + z_c A_{11}^{-1} A_{12} \right]' \Sigma \left[\begin{pmatrix} x \\ y \end{pmatrix} + z_c A_{11}^{-1} A_{12} \right] = 1 \qquad \text{(A. 8)}$$

where

$$\Sigma = \frac{A_{11}}{1 - \frac{z_c^2}{r_1^2 \sin^2 p_1 + r_2^2 \sin^2 p_2 + r_3^2 \sin^2 p_3}}$$

The inverse of the square root of the eigenvalues of Σ are the corresponding radii of the ellipse. Therefore the diameters can be obtained as

$$d_{1,2}^2 = \frac{8 \left(1 - \frac{z_c^2}{r_1^2 \sin^2 p_1 + r_2^2 \sin^2 p_2 + r_3^2 \sin^2 p_3} \right)}{\left(\frac{\cos^2 p_1}{r_1^2} + \frac{\cos^2 p_2}{r_2^2} + \frac{\cos^2 p_3}{r_3^2} \right) \pm \sqrt{\left(\frac{\cos^2 p_1}{r_1^2} + \frac{\cos^2 p_2}{r_2^2} + \frac{\cos^2 p_3}{r_3^2} \right)^2 - 4 \left(\frac{\sin^2 p_1}{r_2^2 r_3^2} + \frac{\sin^2 p_2}{r_1^2 r_3^2} + \frac{\sin^2 p_3}{r_1^2 r_2^2} \right)}}$$

(3) Based on the above equation we can conclude that z_c satisfies the following condition when the cutting plane intersects the ellipsoid.

$$|z_c| \leq \sqrt{r_1^2 \sin^2 p_1 + r_2^2 \sin^2 p_2 + r_3^2 \sin^2 p_3}$$

APPENDIX B: PROOF OF THEOREM 2

Under Assumption (iii), p_i and p_j are a sequence of exchangeable random variables. Therefore $f(p_i)$ and $f(p_i|p_j)$ have the unchanged forms for any permutation of indices $1, 2$ and 3. For convenience, we only need to derive $f(p_3)$, $f(p_2|p_3)$ and $f(p_1|p_3)$. Note that here p_1, p_2 and p_3 satisfy the constraint of (A. 6).

(1) Derivation of $f(p_3)$.

For a uniform orientation, the endpoint of the semi-principal axis $\boldsymbol{r_3}$ uniformly distributed on the surface of the semi-sphere ($z \geq 0$ or $0 \leq p_3 \leq \pi/2$) of radius r_3. Therefore the density function at each point of the surface is $\frac{1}{A}$ where $A = 2\pi r_3^2$ is the surface area. Based on the geometry, we get

$$f(p_3)dp_3 = \frac{dA}{A} = \frac{(2\pi r \cos p_3)(r dp_3)}{2\pi r_3^2} = \cos p_3 \, dp_3 \qquad \text{(B. 1)}$$

Therefore $f(p_3) = \cos p_3$, $p_3 \in [0, \pi/2]$. Alternatively, this density can be easily obtained based on the fact that $f(p_3)$ is proportional to the perimeter of the latitude p_3, i.e., $2\pi r_3 \cos p_3$.

(2) Derivation of $f(p_2|p_3)$.

Since the rotation of the ellipsoid along the $\boldsymbol{z}$ axis does not change the angles $p_i, i = 1,2,3$ and their relationship, for the sake of simplicity, we assume that $\boldsymbol{r_3}$ is in the XZ plane, i.e., $\theta_3 = 0$, as shown in Figure B1. Then the $\boldsymbol{y}$ axis is on the plane containing $\boldsymbol{r}_1$ and $\boldsymbol{r}_2$.

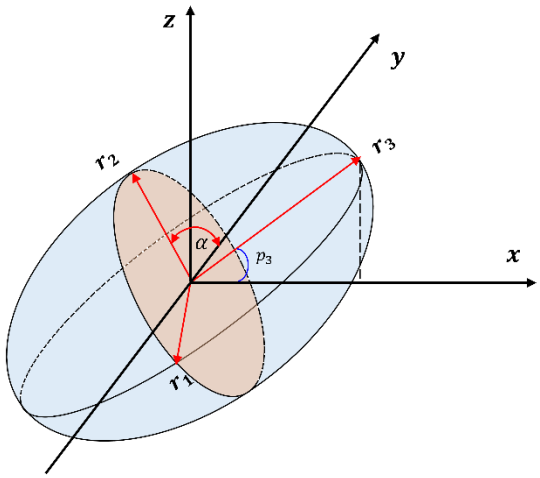

Figure B1 Illustration of an ellipsoid with $\boldsymbol{\theta_3 = 0}$

Define α as the angle between $\boldsymbol{r}_2$ and $\boldsymbol{y}$ axis. Based on the assumption of uniformly distributed orientation,

$$\alpha \sim \text{Uniform}[0, \pi] \tag{B. 2}$$

The endpoint of $\boldsymbol{r_2}$ can be obtained by rotating the point $(0, r_2, 0)$ along the axis $\boldsymbol{r}_3$ by angle α. Using coordinates transformation, $\boldsymbol{r_2}$ can be easily obtained as

$$\boldsymbol{r}_2 = (-r_2 \sin p_3 \sin \alpha\,, r_2 \cos \alpha\,, r_2 \cos p_3 \sin \alpha)$$

Therefore

$$\sin \alpha = \frac{\sin p_2}{\cos p_3} \tag{B. 3}$$

Note that for a general case where $\theta_3 \neq 0$, α is the angle between $\boldsymbol{r}_2$ and the intersection of $\boldsymbol{r}_1$-$\boldsymbol{r}_2$ plane and XY plane. The angle between $\boldsymbol{r}_1$-$\boldsymbol{r}_2$ plane and XY plane can be obtained as $\frac{\pi}{2} - p_3$. Based on this angle, we can also obtain the same result. Based on Equation (B. 3), (B. 3) and variable transformation, the density function $f(p_2|p_3)$ can be calculated as

$$f(p_2|p_3) = \frac{2}{\pi} \frac{1}{\sqrt{1 - \frac{\sin^2 p_2}{\cos^2 p_3}}} \frac{\cos p_2}{\cos p_3} = \frac{2}{\pi} \frac{\cos p_2}{\sin p_1} \tag{B. 4}$$

Since $p_1 = \arcsin \sqrt{1 - \sin^2 p_2 - \sin^2 p_3}$, using variable transformation, we can get

$$f(p_1|p_3) = \frac{2}{\pi} \frac{\cos p_1}{\sin p_2} \tag{B. 5}$$

APPENDIX C: CALCULATION OF p_1 AND z_c

Denote

$$C_1 = \sum_{i=1}^{3} r_i^2 \sin^2 p_i = (r_1^2 - r_2^2)\sin^2 p_1 + (r_3^2 - r_2^2)\sin^2 p_3 + r_2^2 \quad \text{(C. 1)}$$

and

$$C_2 = \sum_{i=1}^{3} \frac{cos^2 p_i}{r_i^2} = \left(\frac{1}{r_2^2} - \frac{1}{r_1^2}\right)\sin^2 p_1 + \left(\frac{1}{r_2^2} - \frac{1}{r_3^2}\right)\sin^2 p_3 + \left(\frac{1}{r_1^2} + \frac{1}{r_3^2}\right) \quad \text{(C. 2)}$$

Based on Equation (1),

$$\frac{C_1}{C_2^2} = \frac{d_1^2 d_2^2 r_1^2 r_2^2 r_3^2}{(d_1^2 + d_2^2)^2} \quad \text{(C. 3)}$$

Combing Equation (C. 1), (C. 2) and (C. 3) we can get

$$C_2^2 \frac{d_1^2 d_2^2 r_1^2 r_2^2 r_3^4}{(d_1^2 + d_2^2)^2} - C_2 r_1^2 r_2^2 r_3^2 + \sin^2 p_3 \left[(r_3^2 - r_1^2)(r_2^2 - r_3^2)\right] + r_1^2 r_2^2 = 0 \quad \text{(C. 4)}$$

Therefore C_2 is one of the roots of Equation (C. 4). Since there are two roots, C_2 is the one satisfying the following constraints based on Equation (C. 2)

$$\frac{1}{r_2^2} + \frac{1}{r_3^2} \le C_2 \le \frac{1}{r_1^2} + \frac{1}{r_2^2}$$

C_1 and p_1 can be calculated once C_2 is obtained. For z_c, based on Equation (1), we can derive that $d_1^2 d_2^2 = \frac{64\left(1 - \frac{z_c^2}{C_1}\right)^2}{4C_1 / r_1^2 r_2^2 r_3^2}$.

Therefore

$$z_c = \sqrt{\left(1 - \frac{\sqrt{C_1} d_1 d_2}{4 r_1 r_2 r_3}\right) C_1}$$

APPENDIX D: CALCULATION OF THE DETERMINANT OF JACOBIAN MATRIX *J*

Let $C_3 = C_2 + \sqrt{C_2^2 - \frac{4C_1}{r_1^2 r_2^2 r_3^2}}$, $C_4 = C_2 - \sqrt{C_2^2 - \frac{4C_1}{r_1^2 r_2^2 r_3^2}}$ where C_1 and C_2 are defined in Equation (C. 1) and (C. 2). $C_1' = (r_1^2 - r_2^2)\sin 2p_1$, $C_2' = \left(\frac{1}{r_2^2} - \frac{1}{r_1^2}\right)\sin 2p_1$, and

$$C_3' = C_2' + \frac{2C_2C_2' - 4C_1'/r_1^2 r_2^2 r_3^2}{2\sqrt{C_2^2 - 4C_1/r_1^2 r_2^2 r_3^2}}, C_4' = C_2' - \frac{2C_2C_2' - 4C_1'/r_1^2 r_2^2 r_3^2}{2\sqrt{C_2^2 - 4C_1/r_1^2 r_2^2 r_3^2}}$$

Denote $\frac{\partial(d_1,d_2)}{\partial(p_1,z_c)} = \begin{bmatrix} j_{11} & j_{12} \\ j_{21} & j_{22} \end{bmatrix}$, then

$$j_{11} = \frac{\partial d_1}{\partial p_1} = \frac{1}{2d_1C_3^2}\left[8\left(\frac{z_c^2C_1'}{C_1^2}\right)C_3 - 8\left(1 - \frac{z_c^2}{C_1}\right)C_3'\right]$$

$$j_{21} = \frac{\partial d_2}{\partial p_1} = \frac{1}{2d_2C_4^2}\left[8\left(\frac{z_c^2C_1'}{C_1^2}\right)C_4 - 8\left(1 - \frac{z_c^2}{C_1}\right)C_4'\right]$$

$$j_{12} = \frac{\partial d_1}{\partial z_c} = \frac{-16z_c/C_1}{2d_1C_3}, j_{22} = \frac{\partial d_2}{\partial z_c} = \frac{-16z_c}{2d_2C_1C_4}$$

$$J = \begin{vmatrix} j_{11} & j_{12} \\ j_{21} & j_{22} \end{vmatrix} = \frac{4z_c}{d_1d_2C_1C_3C_4}[d_1^2C_3' - d_2^2C_4']$$

$$= \frac{4z_c}{d_1d_2C_1C_3C_4}\left[C_2'(d_1^2 - d_2^2) + \frac{\left(2C_2C_2' - \frac{4C_1'}{r_1^2r_2^2r_3^2}\right)(d_1^2 + d_2^2)}{C_3 - C4}\right]$$

Plug in $\frac{C_1}{C_2^2} = \frac{d_1^2d_2^2r_1^2r_2^2r_3^2}{\left(d_1^2+d_2^2\right)^2}$ and $C_3 - C4 = 2C_2\frac{d_2^2-d_1^2}{d_1^2+d_2^2}$ we can get

$$J = \frac{4z_c}{d_1d_2C_1C_3C_4}\left[C_2'(d_1^2 - d_2^2) + \frac{2C_2C_2'(d_1^2 + d_2^2)}{2C_2\frac{d_2^2 - d_1^2}{d_1^2 + d_2^2}} - \frac{\frac{4C_1'}{r_1^2r_2^2r_3^2}(d_1^2 + d_2^2)}{2C_2\frac{d_2^2 - d_1^2}{d_1^2 + d_2^2}}\right]$$

$$= \frac{2d_1d_2r_1^2r_2^2r_3^2z_c}{(d_2^2 - d_1^2)C_1^3}[2C_1C_2' - C_2C_1']$$

APPENDIX E: PROOF OF INEQUILITIES (24)

Based on Equation (1), it is easy to show that (i) d_1 and d_2 reaches the maximum for any given $\{r_i, p_i, i = 1,2,3\}$ when $z_c = 0$; (ii) when $z_c = 0$, for any given p_3, d_1 reaches the maximum while d_2 reaches the minimum at $p_2 = 0$. Similarly, when $z_c = 0$, for any given p_3, d_2 reaches the maximum while d_1 reaches the minimum at $p_2 = \frac{\pi}{2} - p_3$. Therefore

$$d_1^2 \le \frac{8}{\frac{C_1}{r_1^2 r_3^2} + \frac{1}{r_2^2} + \left|\frac{C_1}{r_1^2 r_3^2} - \frac{1}{r_2^2}\right|} \tag{E. 1}$$

$$d_2^2 \le \frac{8}{\frac{C_2}{r_2^2 r_3^2} + \frac{1}{r_1^2} - \left|\frac{C_2}{r_2^2 r_3^2} - \frac{1}{r_1^2}\right|} \tag{E. 2}$$

where $C_1 = (r_3^2 - r_1^2)\sin^2 p_3 + r_1^2$ and $C_2 = (r_3^2 - r_2^2)\sin^2 p_3 + r_2^2$. Since $\sin^2 p_3 \le 1 \le \frac{r_2^2(r_3^2 - r_1^2)}{r_1^2(r_3^2 - r_2^2)}$, $\frac{C_2}{r_2^2 r_3^2} \le \frac{1}{r_1^2}$. Based on (E. 2) we can get

$$d_2 \le \frac{2}{\sqrt{\left(\frac{1}{r_2^2} - \frac{1}{r_3^2}\right) sin^2 p_3 + \frac{1}{r_3^2}}} \le 2r_3 \tag{E. 3}$$

From (E. 3) we can get

$$r_3 \ge \frac{d_2}{2}, r_2 \ge \frac{\sin p_3}{\sqrt{\left(\frac{4}{d_2^2} - \frac{\cos^2 p_3}{r_3^2}\right)}} \tag{E. 4}$$

Similarly, if $\sin^2 p_3 \ge \frac{r_1^2(r_3^2 - r_2^2)}{r_2^2(r_3^2 - r_1^2)}$ or equivalently $r_1 \le \frac{r_2 r_3 \sin p_3}{\sqrt{r_3^2 - r_2^2 \cos^2 p_3}} \le r_2$, based on (E. 1)

$$d_1 \le \frac{2}{\sqrt{\left(\frac{1}{r_1^2} - \frac{1}{r_3^2}\right)\sin^2 p_3 + \frac{1}{r_3^2}}} \le 2r_2 \tag{E. 5}$$

Otherwise, i.e., $\sin^2 p_3 < \frac{r_1^2(r_3^2 - r_2^2)}{r_2^2(r_3^2 - r_1^2)}$

$$d_1 < 2r_2 \tag{E. 6}$$

Therefore

$$r_2 \geq \frac{d_1}{2}, r_1 \geq \frac{\sin p_3}{\sqrt{\left(\frac{4}{d_1^2} - \frac{\cos^2 p_3}{r_3^2}\right)}} \qquad \text{(E. 7)}$$

Base on (E. 4) and (E. 7) we can get the inequalities (26).

APPENDIX F: PROOF OF THEOREM 3

Since the ellipsoidal particles are uniformly distributed on both sides of the image plane, we could limit the analysis to one side, as shown in Figure F1. Divide the specimen on the right side of the image into equally spaced cells with a sufficiently small thickness δ. Suppose the upper bound of the ellipsoid size r_3 is r_{max}, which can be infinite if no upper bound is specified. So we only need to focus the right side of largest distance r_{max} to the image plane. Particles with distance larger than r_{max} to the image plane will not be shown.

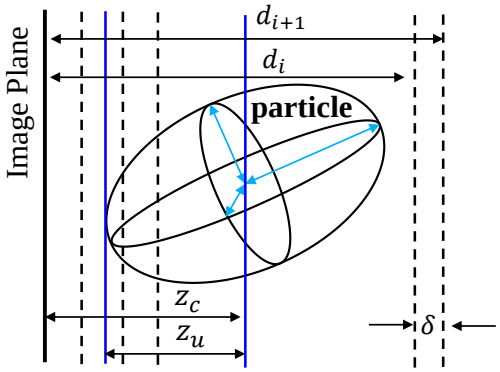

Figure F1. Modeling the ellipsoidal particles on an image as an inhomogeneous Poisson process

Denote the number of particles that are on the image and whose distance is within d_i by $N(d_i)$, and denote the number of particles shown on the image coming from the *i*th cell by $N_i = N(d_i) - N(d_{i-1})$ with $N_0 = d_0 = 0$. Then we have

(1) $N(0) = 0$ by definition
(2) $N_1, N_2, \ldots$ are independent under the assumption of CSR
(3) $N_i, i = 1, \ldots$ have the Poisson distribution with rate $A\delta\lambda_0 Pr(z_u \geq z_c)$ where A is the area of the image plane, λ_0 is the particle density in the 3D space.
(4) For $\delta \to 0$, the Poisson rate for $N_i, i \geq 1$ is $A\delta\lambda_0 Pr(z_u \geq d_i)$, therefore

$$\lim_{\delta \to 0} \frac{\Pr(N_i = 1)}{\delta} = A\lambda_0 Pr(z_u \geq d_i), \lim_{\delta \to 0} \frac{\Pr(N_i > 1)}{\delta} = 0$$

Based on (1-4) we know the particles shown on the image from the right size is an inhomogeneous Poisson process with rate function $\lambda(d) = A\lambda_0 Pr(z_u \geq d)$.

$$\lambda(d) = A\lambda_0 \int_d^{r_{max}} f_{z_u}(r)dr$$

The total number of particles shown on the intersectional image follows a Poisson distribution with Poisson parameter

$$\lambda = 2\int_0^{r_m} \lambda(x)\,dx = 2A\lambda_0 \int_0^{r_{max}} \int_x^{r_{max}} f_{z_u}(r)\,dr\,dx = 2A\lambda_0 \int_0^{r_{max}} \int_0^{r} f_{z_u}(r)\,dx\,dr$$
$$= 2A\lambda_0 \int_0^{r_{max}} r f_{z_u}(r)\,dr = 2A\lambda_0 \overline{z_u}$$

Note that r_{max} can be set to infinite if no upper bound is specified.

APPENDIX G: PROOF OF THEOREM 4

The volume fraction is $\rho = \frac{\sum_{i=1}^{N} V_i}{V}$ where V_i is the volume of *i*th ellipsoid, N is the total number of ellipsoids and $N \sim \text{Poisson}(\lambda_0 V)$. Therefore $\sum_{i=1}^{N} V_i$ follows a compound Poisson distribution. The mean and variance can be calculated based on the compound Poisson distribution as

$$E(\rho) = \frac{E(N)E(V_e)}{V} = \lambda_0 E(V_e)$$

$$Var(\rho) = \frac{E(N)E(V_e^2)}{V^2} = \frac{\lambda_0 E(V_e^2)}{V}$$

Based on the lognormal and beta distribution,

$$E(V_e) = \frac{4\pi}{3} E(r_3^3 * r_{a2}^2 * r_{a1}) = \frac{4\pi}{3} E(r_3^3)E(r_{a2}^2)E(r_{a1})$$
$$= \frac{4\pi}{3} \frac{\alpha_1}{\alpha_1 + \beta_1} \frac{\alpha_2\beta_2 + \alpha_2^2(\alpha_2 + \beta_2 + 1)}{(\alpha_2 + \beta_2)^2(\alpha_2 + \beta_2 + 1)} \exp(3\mu + \frac{9}{2}\sigma^2)$$

where $r_{a1} = r_1/r_2$ and $r_{a2} = r_2/r_3$

$$E(V_e^2) = \frac{16\pi^2}{9} E(r_3^6) E(r_{a2}^4) E(r_{a1}^2)$$
$$= \frac{32\pi^2}{3} \frac{\alpha_1\beta_1 + \alpha_1^2(\alpha_1+\beta_1+1)}{(\alpha_1+\beta_1)^2(\alpha_1+\beta_1+1)} \frac{[\alpha_2^3 + \alpha_2^2(1-2\beta_2) + \beta_2^2(1+\beta_2) - 2\alpha_2\beta_2(2+\beta_2)]}{\alpha_2\beta_2(\alpha_2+\beta_2+2)(\alpha_2+\beta_2+3)} \exp(6\mu + 18\sigma^2)$$

APPENDIX H: PROOF OF THEOREM 5

Let S and V_e denote the cross-section area and volume of an ellipsoid with the cutting plane. Then

$$E(S) = E(S|I=1,\boldsymbol{\theta})P(I=1|\boldsymbol{\theta}) + E(S|I=0,\boldsymbol{\theta})P(I=0|\boldsymbol{\theta})$$

$$= E\left(\frac{\pi\left(1-\frac{z_c^2}{z_u^2}\right) r_1 r_2 r_3}{z_u} \middle| I=1,\boldsymbol{\theta} \right) P(I=1|\boldsymbol{\theta}) = \pi E\left(1-\frac{z_c^2}{z_u^2}\right) E\left(\frac{r_1 r_2 r_3}{z_u}\middle| I=1,\boldsymbol{\theta}\right) P(I=1|\boldsymbol{\theta})$$

$$= E\left(\frac{V_e}{2z_u}\middle| I=1,\boldsymbol{\theta}\right) P(I=1|\boldsymbol{\theta})$$

$$= \int \frac{V_e}{2z_u} f(r_1,r_2,r_3,p_3,p_2|I=1,\boldsymbol{\theta}) d(r_1,r_2,r_3,p_3,p_2) P(I=1|\boldsymbol{\theta})$$

$$= \int \frac{V_e}{2z_u} \frac{f(r_1,r_2,r_3,p_3,p_2|\boldsymbol{\theta})\frac{z_u}{r_{max}}}{P(I=1|\boldsymbol{\theta})} d(r_1,r_2,r_3,p_3,p_2) P(I=1|\boldsymbol{\theta})$$

$$= \int \frac{V_e}{2r_{max}} f(r_1,r_2,r_3,p_3,p_2|\boldsymbol{\theta})\, d(r_1,r_2,r_3,p_3,p_2) = \frac{E(V_e|\boldsymbol{\theta})}{2r_{max}}$$

Therefore

$$E(S) = \frac{E(V_e|\boldsymbol{\theta})}{2r_{max}}$$

$$E(\rho) = E\left(\frac{\sum_{i=1}^N V_i}{2Ar_{max}}\right) = E\left(\frac{\sum_{i=1}^N S_i}{A}\right) = \frac{A_v}{A}$$

where V_i and S_i are the volume and cross-sectional area of ellipsoid i, respectively, and N is the total number of ellipsoids in the two sides of the cutting plane of maximum distance r_{max}.

APPENDIX I: SAMPLING THE ORIENTATION ANGLES p_1, p_2AND p_3

The inverse transform sampling can be used to sample p_1, p_2 and p_3. The orientation angles p_1, p_2 and p_3 have the following distributions according to Theorem 2:

$$f(p_i) = \cos p_i \,, f(p_i|p_j) = \frac{2}{\pi}\frac{\cos p_i}{\sin p_k}, (i,j,k) \in \text{Perm}(1,2,3)$$

where $\sin^2 p_1 + \sin^2 p_2 + \sin^2 p_3 = 1$. The cumulative distribution function (CDF) of p_3 is $\sin p_3$. The CDF of p_1 given p_3 is calculated as follows.

$$\Pr(p_2 \le x|p_3) = \int_0^x \frac{2}{\pi}\frac{\cos p_2}{\sin p_1}\,dp_2 = \int_0^x \frac{2}{\pi}\frac{\cos p_2}{\sin p_1}\,dp_2 = \int_0^{\sin x} \frac{2}{\pi}\frac{dt}{\sqrt{\cos^2 p_3 - t^2}}$$

$$= \frac{2}{\pi}\arcsin\frac{\sin x}{\cos p_3} \text{ for } x \in [0, \pi/2 - p_3]$$

Therefore (p_1, p_2, p_3) can be sampled as follows:

- Sample $y_1 \sim U[0,1]$ and set $p_3 = \operatorname{asin} y_1$
- Sample $y_2 \sim U[0,1]$ and set $p_2 = \operatorname{asin}\left(\cos p_3 \sin\frac{\pi y_2}{2}\right)$
- Calculate $p_1 = \operatorname{asin}\sqrt{1 - \sin^2 p_2 - \sin^2 p_3}$

REFERENCES

[1] J. A. Slotwinski, E. J. Garboczi, and K. M. Hebenstreit, "Porosity Measurements and Analysis for Metal Additive Manufacturing Process Control," *JOURNAL OF RESEARCH OF THE NATIONAL INSTITUTE OF STANDARDS AND TECHNOLOGY,* vol. 119, pp. 494-528, 2014.

[2] N. T. Aboulkhair, N. M. Everitt, I. Ashcroft, and C. Tuck, "Reducing porosity in AlSi10Mg parts processed by selective laser melting," *Additive Manufacturing,* vol. 1, pp. 77-86, 2014.

[3] K. Kempen, L. Thijs, E. Yasa, M. Badrossamay, W. Verheecke, and J. Kruth, "Process optimization and microstructural analysis for selective laser melting of AlSi10Mg," in *Solid Freeform Fabrication Symposium*, 2011, pp. 484-495.

[4] H. Gong, "Generation and detection of defects in metallic parts fabricated by selective laser melting and electron beam melting and their effects on mechanical properties," *Electronic Theses and Dissertations,* 2013.

[5] L. Murr, E. Martinez, S. Gaytan, D. Ramirez, B. Machado, P. Shindo, J. Martinez, F. Medina, J. Wooten, and D. Ciscel, "Microstructural architecture, microstructures, and mechanical properties for a nickel-base superalloy fabricated by electron beam melting," *Metallurgical and Materials Transactions A,* vol. 42, pp. 3491-3508, 2011.

[6] D. Buchbinder, H. Schleifenbaum, S. Heidrich, W. Meiners, and J. Bültmann, "High power selective laser melting (HP SLM) of aluminum parts," *Physics Procedia,* vol. 12, pp. 271-278, 2011.

[7] E. Santos, F. Abe, Y. Kitamura, K. Osakada, and M. Shiomi, "Mechanical properties of pure titanium models processed by selective laser melting," *Proceedings of the Solid,* 2002.

[8] S. Li, L. Murr, X. Cheng, Z. Zhang, Y. Hao, R. Yang, F. Medina, and R. Wicker, "Compression fatigue behavior of Ti–6Al–4V mesh arrays fabricated by electron beam melting," *Acta Materialia,* vol. 60, pp. 793-802, 2012.

[9] J.-P. Kruth, L. Froyen, J. Van Vaerenbergh, P. Mercelis, M. Rombouts, and B. Lauwers, "Selective laser melting of iron-based powder," *Journal of Materials Processing Technology,* vol. 149, pp. 616-622, 2004.

[10] J. Wu, S. Zhou, and X. Li, "Acoustic Emission Monitoring for Ultrasonic Cavitation Based Dispersion Process," *Journal of Manufacturing Science and Engineering,* vol. 135, p. 031015, 2013.

[11] J. Wu, S. Zhou, and X. Li, "Ultrasonic Attenuation Based Inspection Method for Scale-up Production of A206–Al2O3 Metal Matrix Nanocomposites," *Journal of Manufacturing Science and Engineering,* vol. 137, p. 011013, 2015.

[12] J. Wu, Y. Liu, and S. Zhou, "Bayesian Hierarchical Linear Modeling of Profile Data With Applications to Quality Control of Nanomanufacturing."

[13] Y. Liu, J. Wu, S. Zhou, and X. Li, "Microstructure Modeling and Ultrasonic Wave Propagation Simulation of A206–Al2O3 Metal Matrix Nanocomposites for Quality Inspection," *Journal of Manufacturing Science and Engineering,* vol. 138, p. 031008, 2016.

[14] J. C. Russ, *The image processing handbook*: CRC press, 2015.

[15] H. Liu, S. Zhou, and X. Li, "Inferring the Size Distribution of 3D Particle Clusters in Metal Matrix Nanocomposites," *Journal of Manufacturing Science and Engineering,* vol. 135, p. 011013, 2013.

[16] Q. Zhou, J. Zhou, M. De Cicco, S. Zhou, and X. Li, "Detecting 3D spatial clustering of particles in nanocomposites based on cross-sectional images," *Technometrics,* vol. 56, pp. 212-224, 2014.

[17] J. Wu, Y. Yuan, and X. Li, "Size Distribution Estimation of Three-Dimensional Particle Clusters in Metal-Matrix Nanocomposites Considering Sampling Bias," *Journal of Manufacturing Science and Engineering,* vol. 139, pp. 081017-081017-11, 2017.

[18] P. J. Diggle, *Statistical analysis of spatial and spatio-temporal point patterns*: CRC Press, 2013.

[19] P. P. Klein, "On the ellipsoid and plane intersection equation," *Applied Mathematics,* vol. 3, p. 1634, 2012.

[20] M. R. Gupta and Y. Chen, *Theory and use of the EM algorithm*: Now Publishers Inc, 2011.

[21] E. Babinsky and P. Sojka, "Modeling drop size distributions," *Progress in energy and combustion science,* vol. 28, pp. 303-329, 2002.

[22] E. Limpert, W. A. Stahel, and M. Abbt, "Log-normal Distributions across the Sciences: Keys and Clues," *BioScience,* vol. 51, 2001.

[23] L. Kiss, J. Söderlund, G. Niklasson, and C. Granqvist, "New approach to the origin of lognormal size distributions of nanoparticles," *Nanotechnology,* vol. 10, p. 25, 1999.

[24] G. C. Wei and M. A. Tanner, "A Monte Carlo implementation of the EM algorithm and the poor man's data augmentation algorithms," *Journal of the American Statistical Association,* vol. 85, pp. 699-704, 1990.

[25] P. L'Ecuyer and C. Lemieux, "Recent advances in randomized quasi-Monte Carlo methods," in *Modeling uncertainty*, ed: Springer, 2005, pp. 419-474.

[26] J. H. Halton, "On the efficiency of certain quasi-random sequences of points in evaluating multi-dimensional integrals," *Numerische Mathematik,* vol. 2, pp. 84-90, 1960.

[27] I. y. M. Sobol', "On the distribution of points in a cube and the approximate evaluation of integrals," *Zhurnal Vychislitel'noi Matematiki i Matematicheskoi Fiziki,* vol. 7, pp. 784-802, 1967.

[28] J. Kennedy and R. Eberhart, "Particle swarm optimization," in *Neural Networks, 1995. Proceedings., IEEE International Conference on*, 1995, pp. 1942-1948.

[29] S. I. Resnick, *Adventures in stochastic processes*: Springer Science & Business Media, 2013.

[30] P. J. Bickel and K. A. Doksum, *Mathematical statistics: basic ideas and selected topics* vol. 2: CRC Press, 2015.

[31] C. Weingarten, D. Buchbinder, N. Pirch, W. Meiners, K. Wissenbach, and R. Poprawe, "Formation and reduction of hydrogen porosity during selective laser melting of AlSi10Mg," *Journal of Materials Processing Technology,* vol. 221, pp. 112-120, 2015.

[32] S. A. Khairallah, A. T. Anderson, A. Rubenchik, and W. E. King, "Laser powder-bed fusion additive manufacturing: Physics of complex melt flow and formation mechanisms of pores, spatter, and denudation zones," *Acta Materialia,* vol. 108, pp. 36-45, 2016.

[33] M. Kabir and H. Richter, "Modeling of Processing-Induced Pore Morphology in an Additively-Manufactured Ti-6Al-4V Alloy," *Materials,* vol. 10, p. 145, 2017.

[34] T. Vilaro, C. Colin, and J.-D. Bartout, "As-fabricated and heat-treated microstructures of the Ti-6Al-4V alloy processed by selective laser melting," *Metallurgical and Materials Transactions A,* vol. 42, pp. 3190-3199, 2011.

[35] X. Zhou, D. Wang, X. Liu, D. Zhang, S. Qu, J. Ma, G. London, Z. Shen, and W. Liu, "3D-imaging of selective laser melting defects in a Co–Cr–Mo alloy by synchrotron radiation micro-CT," *Acta Materialia,* vol. 98, pp. 1-16, 2015.

[36] H. Rieder, A. DillHofer, M. Spies, J. Bamberg, and T. Hess, "Online monitoring of additive manufacturing processes using ultrasound," *ECNDT 2014*, 2014.

[37] J. M. Waller, B. H. Parker, K. L. Hodges, E. R. Burke, J. L. Walker, and E. R. Generazio, "Nondestructive Evaluation of Additive Manufacturing," 2014.

[38] H. Park and K. Miwa, "X-ray computed tomography for micro porosity in AZ91D alloy," *Materials Transactions*, vol. 44, pp. 2326-2333, 2003.

[39] P. M. Dixon, "Ripley's K function," *Encyclopedia of environmetrics*, 2002.